People's Democratic Republic of Algeria

Ministry of Higher Education and Scientific Research

Ecole Nationale Polytechnique

المدرسة الوطنية المتعددة التقنيات
Ecole Nationale Polytechnique

Metallurgy Department

End-of-Studies Project Report

for the attainment of the State Engineer's diploma in

Material engineering

Influence of Electrical Current on the Microstructure and Mechanical Properties of Steel Welds: A Study Using Submerged Arc Welding (SAW) Method

---

Presented by: **CHOUKHA Abdelouahab**

Under the supervision of: **Pr. CHITROUB Mohamed**

Presented and publicly supported on (22/06/2024)

Composition of the Jury:

President	KASSER Abdelmadjid	Phd	ENP
Supervisor	CHITROUB Mohamed	professor	ENP
Examiner	BOUHAFS Chouayb	MCB	ENP

ENP 2024

People's Democratic Republic of Algeria

Ministry of Higher Education and Scientific Research

Ecole Nationale Polytechnique

المدرسة الوطنية المتعددة التقنيات
Ecole Nationale Polytechnique

Metallurgy Department

End-of-Studies Project Report

for the attainment of the State Engineer's diploma in

Material engineering

Influence of Electrical Current on the Microstructure and Mechanical Properties of Steel Welds: A Study Using Submerged Arc Welding (SAW) Method

---

Presented by: **CHOUKHA Abdelouahab**

Under the supervision of: **Pr. CHITROUB Mohamed**

Presented and publicly supported on (22/06/2024)

Composition of the Jury:

President	KASSER Abdelmadjid	Phd	ENP
Supervisor	CHITROUB Mohamed	professor	ENP
Examiner	BOUHAFS Chouayb	MCB	ENP

ENP 2024

République Algérienne Démocratique et Populaire
Ministère de l'Enseignement Supérieur et de la Recherche Scientifique

Ecole Nationale Polytechnique

المدرسة الوطنية المتعددة التقنيات
Ecole Nationale Polytechnique

Département : Métallurgie

Mémoire de projet de fin d'études

Pour l'obtention du diplôme d'Ingénieur d'État en

Génie des matériaux

Influence du courant électrique sur la microstructure et les propriétés mécaniques des soudures en acier : une étude utilisant la méthode de soudage à l'arc submergé (SAW)

Réalisé par : **CHOUKHA Abdelouahab**

Sous la direction de : **Pr. CHITROUB Mohamed**

Présenté et soutenu publiquement le (22/06/2024)

Composition du jury :

Président	KASSER Abdelmadjid	Phd	ENP
Promoteur	CHITROUB Mohamed	professeur	ENP
Examinateur	BOUHAFS Chouayb	MCB	ENP

ENP 2024

ملخص

تستكشف هذه الدراسة تأثير التيارات الكهربائية المتفاوتة على البنية المجهرية والخواص الميكانيكية للحامات الفولاذ، باستخدام طريقة اللحام بالقوس المغمور . أُجريت التجارب باستخدام تيارات 280 أمبير و310 أمبير و350 أمبير و390 أمبير. خضعت العينات الملحومة لفحوصات ماكروسكوبية ومجهرية، واختبارات ميكانيكية (اختبارات الصلابة الدقيقة واختبارات الشد)، وتحليلات متقدمة باستخدام الفحص المجهري الإلكتروني الماسح والانبعاثات المجهرية بالأشعة السينية. أظهرت النتائج أن زيادة تيار اللحام يؤثر بشكل كبير على التحولات البنيوية المجهرية والسلوك الميكانيكي للحامات. يوفر هذا البحث رؤى قيمة لتحسين جودة اللحامات الفولاذية وأدائها.

.**الكلمات المفتاحية:** لحام القوس المغمور، لحام الفولاذ، التيار الكهربائي، البنية المجهرية، الخواص الميكانيكية

..

Résumé

Cette étude explore l'impact de la variation des courants électriques sur la microstructure et les propriétés mécaniques des soudures en acier, en utilisant la méthode de soudage à l'arc submergé (SAW). Des expériences ont été menées avec des courants de 280A, 310A, 350A et 390A. Les échantillons soudés ont subi des examens macroscopiques et microscopiques, des tests mécaniques (tests de microdureté et de traction) et des analyses avancées utilisant la microscopie électronique à balayage (SEM) et la diffraction des rayons X (XRD). Les résultats montrent que l'augmentation du courant de soudage affecte de manière significative les transformations microstructurales et le comportement mécanique des soudures. Cette recherche fournit des informations précieuses pour optimiser les paramètres de soudage afin d'améliorer la qualité et les performances des soudures en acier.

Mots-clés : Soudage à l'Arc Submergé (SAW), Soudures en Acier, Courant Électrique, Microstructure, Propriétés Mécaniques.

Abstract

This study explores the impact of varying electrical currents on the microstructure and mechanical properties of steel welds, utilizing the Submerged Arc Welding (SAW) method. Experiments were conducted using currents of 280A, 310A, 350A, and 390A. The welded samples underwent macroscopic and microscopic examinations, mechanical tests (microhardness and tensile tests), and advanced analyses using Scanning Electron Microscopy (SEM) and X-ray Diffraction (XRD). The results demonstrate that increasing welding current significantly affects the microstructural transformations and mechanical behavior of the welds. This research provides valuable insights for optimizing welding parameters to enhance the quality and performance of steel welds.

Keywords: Submerged Arc Welding (SAW), Steel Welds, Electrical Current, Microstructure, Mechanical Properties.

Acknowledgements

First and foremost, I would like to thank God Almighty for granting me the courage, strength, and determination to complete this modest work.

I would like to extend my heartfelt thanks to Pr. Mohamed Chitroub for his unwavering support and guidance throughout the preparation of this thesis. Your mentorship has been invaluable.

I also express my gratitude to Mr. Bouras Youcef and Dr. Behloul Youcef for their assistance and kindness. Your help has been greatly appreciated.

I am deeply thankful to the entire team at BAG Banta, with whom I had the opportunity to share enriching moments. Your support and cooperation have been crucial to this study.

I am also grateful to Mr. KASSER, for agreeing to chair the jury of my defense.

My sincere thanks go to Mr. BOUHAFS for his keen interest in my project, and for agreeing to examine it and be a member of the jury.

Lastly, I would like to thank all the teachers who have helped me and contributed to my education throughout my studies. Your dedication and support have shaped my academic journey.

Dedication

To my dear parents, my loving family, and my precious friends,

This dedication is for you, to tell you how important you are to me. You are the strength that pushes me forward, the smile that brightens my darkest days, and the safe haven in the turmoil of life.

To my parents, thank you for giving me life, education, and unconditional love. You are my first teachers and the guardians of my dreams. You have laid the foundations upon which I build my life, and for that, I will be eternally grateful.

To my family, thank you for being my anchor and my guiding light. Each of you, in your unique way, has contributed to shaping the person I am today. You are the link that connects me to the past while accompanying me toward the future.

And to my friends, thank you for being there for me in moments of joy and in moments of challenge. You are the brothers and sisters I have chosen, the companions on this journey of life.

I dedicate every victory, every achievement, and every moment of happiness to you all. Your support, your love, and your friendship are the greatest gifts I could ever ask for. Together, we face whatever comes our way, and I am convinced that the best is yet to come.

With all my gratitude and love,

Table of Contents

List of abbreviations

SAW - Submerged Arc Welding
HAZ - Heat-Affected Zone
HV - Vickers Hardness
SEM - Scanning Electron Microscopy
EDS - Energy Dispersive Spectroscopy
XRD - X-ray Diffraction
ReH - Upper Yield Strength
Rm - Tensile Strength
A% - Elongation after Fracture
EN - European Standard
BS3 - Grade of Steel
P265NB - Steel Specification
AC - Alternating Current
DC - Direct Current
GPL - Gas Petroleum Liquefied
MPa - Megapascal
T - Temperature
BCC - Body-Centered Cubic
FCC - Face-Centered Cubic
BOF - Basic Oxygen Furnace
EAF - Electric Arc Furnace
Al - Aluminum
Si - Silicon
Mn - Manganese
P - Phosphorus
S - Sulfur
Ni - Nickel
Cu - Copper
Mo - Molybdenum
Ti - Titanium
CaO - Calcium Oxide
SiO_2 - Silicon Dioxide
Fe - Iron
Fe_2O_3 - Iron (III) Oxide (Hematite)
Fe_3O_4 - Iron. (II, III) Oxide (Magnetite)
FeO - Iron (II) Oxide
Fe_3C - Iron Carbide (Cementite)
$CaCO_3$ - Calcium Carbonate
$CaSiO_3$ - Calcium Silicate
CaS - Calcium Sulfide
$Ca_3(PO_4)_2$ - Calcium Phosphate
γ - Gamma (Austenite)
δ - Delta (Ferrite)
α - Alpha (Ferrite)

Figures list

List of tables

General Introduction

General Introduction

Welding is a fundamental process in the manufacturing and construction industries, enabling the joining of materials to create complex structures and components. Among the various welding techniques, Submerged Arc Welding (SAW) stands out for its efficiency and ability to produce high-quality welds. This thesis investigates the influence of electrical current on the microstructure and mechanical properties of steel welds, utilizing the SAW method.

Steel, an alloy primarily composed of iron and carbon, undergoes significant changes in its microstructure and properties when subjected to welding. The microstructural transformations and mechanical behavior of welded joints are crucial for determining their performance in practical applications. Understanding these changes is essential for optimizing welding parameters and improving the quality of welds.

The primary objective of this study is to explore how varying welding currents affect the microstructure and mechanical properties of steel welds. By conducting experiments with different welding currents, we aim to gain insights into the optimal parameters for achieving desired weld qualities. The experiments include macroscopic and microscopic examinations, mechanical tests such as microhardness and tensile tests, and advanced analyses using Scanning Electron Microscopy (SEM) and X-ray Diffraction (XRD).

The research is structured as follows:

Chapter 1: Theoretical Background - This chapter provides a comprehensive overview of the fundamental concepts related to steel manufacturing, welding processes, and the specificities of Submerged Arc Welding (SAW). It includes the iron-carbon phase diagram, the types of welding, and the effects of welding parameters on weld quality.

Chapter 2: Materials and Experimental Techniques - This chapter details the materials used in the study, including the base metal, filler metal, and flux. It describes the welding equipment and procedure, sample preparation, and the various analytical techniques employed to examine the welded samples.

Chapter 3: Results and Discussion - This chapter presents the results of the macroscopic and microscopic examinations, mechanical tests, SEM, EDS, and XRD analyses. The findings are

discussed in the context of how different welding currents influence the microstructure and mechanical properties of the welds.

This study aims to contribute to the existing knowledge on SAW by providing a detailed analysis of the effects of welding current on steel welds. The insights gained from this research will be valuable for industries that rely on welding for the fabrication of steel structures, helping to optimize welding processes and improve the performance and durability of welded joints.

Chapter 1: Theoretical background

Introduction:

The study of steel manufacturing and its subsequent transformation through various processes is fundamental to materials science and engineering. This chapter provides a comprehensive theoretical background on the production of steel sheets, exploring each critical stage from the extraction of raw iron ore to the complex processes involved in steelmaking and alloying. It begins with an in-depth look at the extraction of iron ore, primarily focusing on the most common forms such as hematite and magnetite. This is followed by a detailed examination of the ironmaking process within blast furnaces, where raw iron ore is transformed into pig iron through a series of reduction reactions. The formation of slag, a byproduct that aids in impurity removal, is also discussed.

Furthermore, the chapter delves into primary and secondary steelmaking processes, highlighting methods like the Basic Oxygen Furnace (BOF) and Electric Arc Furnace (EAF) used to refine pig iron into steel. It outlines the significance of deoxidation and alloying in achieving the desired chemical and mechanical properties of steel, providing examples of common deoxidizing agents and alloying elements.

Another pivotal focus of this chapter is the iron-carbon phase diagram, which serves as a crucial tool in understanding the behavior of iron-carbon alloys across different temperatures and compositions. This section explains the various phases such as austenite, ferrite, and cementite, and their transformations which are essential for tailoring the properties of steel for diverse applications. The diagram's relevance extends across numerous industrial sectors, enabling engineers to optimize steel properties for specific uses.

In summary, Chapter 1 lays the groundwork for understanding the complex journey of steel from its raw material state to a finished product, emphasizing the critical processes and theoretical concepts that underpin steel manufacturing and metallurgy.

1.1 steel sheets manufacturing:

The production of sheet metal from iron ore involves several key steps, each with its own set of chemical reactions and processes. This comprehensive journey from raw material to finished product encompasses extraction, purification, alloying, and shaping processes.[5]

1.1.1 Extraction of Iron Ore:

Iron ore primarily consists of iron oxides, with hematite (Fe2O3) and magnetite (Fe3O4) being the most common forms. The extraction of iron from its ore is the first step in the production of steel.[1]

1.1.2 Ironmaking (Blast Furnace Process):

The extracted iron ore is processed in a blast furnace, where it is converted to pig iron. The key reactions in a blast furnace include:

Reduction of Iron Oxides: Iron ore is reduced to iron using carbon (from coke) as the reducing agent. The primary reactions are:

Fe_2O_3+3C $\rightarrow$ 2Fe + 3CO

3Fe_2O_3+ CO$\rightarrow$ 2Fe_3O_4 + CO_2

Fe_3O_4+ CO $\rightarrow$ 3FeO + CO_2

FeO + C $\rightarrow$ Fe + CO

Formation of Slag: Limestone ($CaCO_3$) is added to the furnace to remove impurities in the form of slag.

$CaCO_3$ $\rightarrow$ CaO + CO_2

CaO + $SiO_2$$\rightarrow$ $CaSiO_3$ (slag).[1] [2]

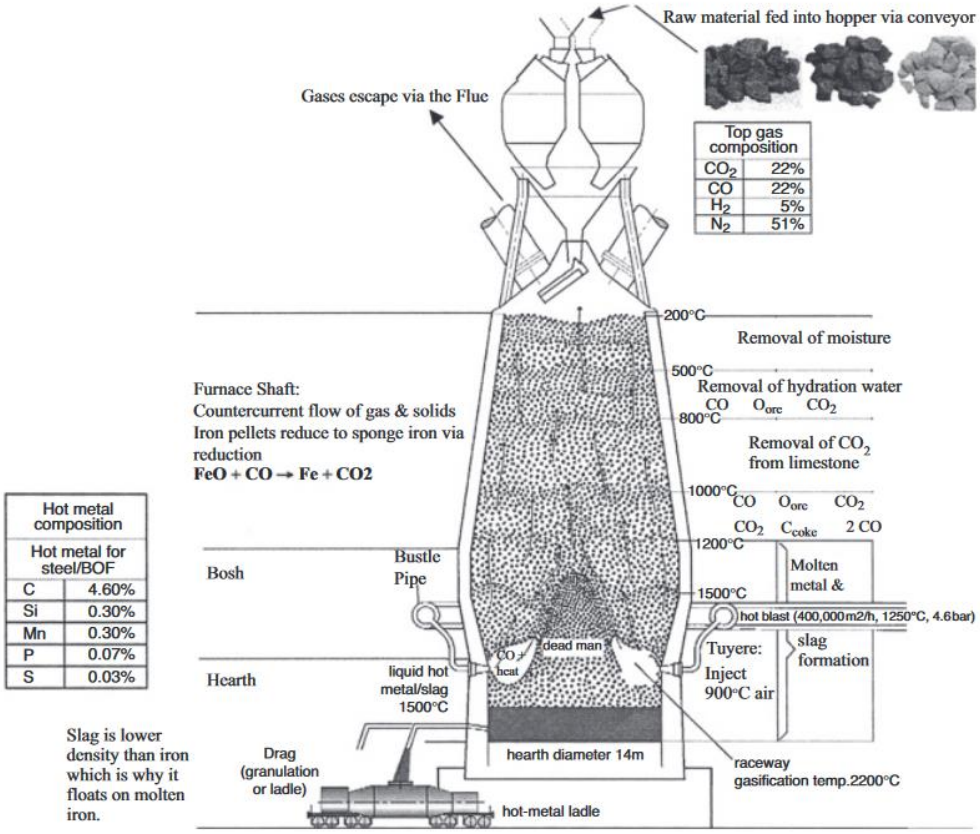

Figure 1. Blast furnace.[1]

1.1.3 Primary Steelmaking:

Pig iron from the blast furnace is refined to reduce its carbon content and remove impurities. Two primary methods are used: Basic Oxygen Furnace (BOF) and Electric Arc Furnace (EAF).

- BOF Process: Oxygen is blown into the molten pig iron to oxidize and remove impurities.

$C+O_2 \rightarrow CO_2$

$Si+O_2 \rightarrow SiO_2$

$P+5O_2 \rightarrow P_2O_5$

- EAF Process: Primarily used for recycling scrap steel, electric arcs melt the scrap in the presence of oxygen to purify it.[1]

1.1.4 Secondary Steelmaking:

Secondary steelmaking is a critical phase in the steel production process that follows primary steelmaking. It involves refining the composition of the steel to achieve the desired chemical and mechanical properties. This stage is essential for producing steel grades that meet specific quality standards and application requirements.

A. Deoxidation:

During the steelmaking process, oxygen can become dissolved in the molten steel, which can lead to the formation of oxides that weaken the steel. Deoxidation is the process of removing excess oxygen from the molten steel to prevent the formation of these detrimental oxides.

- Deoxidation Reactions: Various deoxidizing agents are added to the molten steel to react with the dissolved oxygen and form stable oxides, which can then be removed from the steel. Common deoxidizing agents include aluminum (Al), silicon (Si), and manganese (Mn). The reactions for deoxidation using these elements are as follows:

$2Al + 3O \rightarrow Al_2O_3$ (alumina)

$Si + O_2 \rightarrow SiO_2$ (silica)

$Mn + O \rightarrow MnO$ (manganese oxide)

These reactions result in the formation of solid oxide particles that float to the surface of the molten steel and are removed as part of the slag.[1]

B. Alloying:

Alloying is the process of adding other elements to the molten steel to enhance its properties, such as strength, hardness, corrosion resistance, and toughness. The choice of alloying elements depends on the desired properties of the final steel product.

- Alloying Reactions: While specific reactions for alloying are not typically written as chemical equations, the process involves the dissolution of alloying elements into the molten steel. Examples of alloying elements and their effects include:
  - Chromium (Cr) enhances corrosion resistance and hardenability.
  - Nickel (Ni) improves toughness and strength.
  - Molybdenum (Mo) increases high-temperature strength and hardenability.
  - Vanadium (V) contributes to wear resistance and high-temperature strength.

The addition of these elements is carefully controlled to achieve the desired composition and properties in the final steel product. [3]

C. Slag Formation

During secondary steelmaking, slag also plays a crucial role in refining the steel. Slag is a byproduct that captures impurities and helps in the deoxidation process.

- Slag Formation Reactions: The formation of slag involves the combination of fluxes such as lime (CaO) with impurities like sulfur (S) and phosphorus (P) to form compounds that are not soluble in molten steel.

$CaO+S \rightarrow CaS$ (calcium sulfide)

$3CaO+P_2O_5 \rightarrow Ca_3(PO_4)_2$ (calcium phosphate)

These reactions result in the formation of slag that contains the undesirable impurities, which can then be skimmed off the surface of the molten steel.

Secondary steelmaking is a complex process that requires precise control over temperature, composition, and timing to ensure that the final steel product meets the required specifications. The deoxidation and alloying steps, along with the careful management of slag formation, are essential to producing high-quality steel.[4]

1.1.5 Continuous Casting:

Mold Casting: The refined molten steel is poured into a water-cooled copper mold, forming a solid shell around the liquid steel.

Continuous Withdrawal: As the steel cools and solidifies, it is continuously withdrawn from the bottom of the mold in the form of a continuous strand or slab.

Cutting: The continuous strand is cut into desired lengths to produce semi-finished products such as slabs, blooms, or billets.[6]

1.1.6.Hot Rolling:

The semi-finished products are heated and then hot-rolled to reduce their thickness and to achieve the desired shape and mechanical properties. Hot rolling occurs above the steel's recrystallization temperature, allowing it to be shaped and sized.[1]

1.1.7 Cold Rolling:

For finer thickness and surface quality, steel is further processed through cold rolling, which occurs below the recrystallization temperature. This step enhances the strength and finish of the steel, making it suitable for various applications, including sheet metal production.[1]

1.1.8 Finishing Processes:

A. Heat Treatment:

Annealing: Steel is heated to a specific temperature and then slowly cooled to relieve internal stresses, improve ductility, and refine grain structure.

Quenching: Steel is rapidly cooled by immersion in a quenching medium (usually water, oil, or air) to harden it by transforming austenite into martensite.

Tempering: Hardened steel is reheated to a lower temperature and then cooled again to improve toughness and reduce brittleness.[7]

B. Surface Treatment:

Galvanizing: Steel is coated with a layer of zinc through hot-dip or electroplating methods to provide corrosion resistance.

Coating: Various coatings such as paint, epoxy, or polymer coatings are applied to steel surfaces for protection against corrosion, abrasion, or to enhance aesthetics.

Plating: Steel surfaces may be plated with other metals like chromium, nickel, or tin for improved corrosion resistance and decorative purposes.[8]

C. Final Inspection and Quality Control:

Dimensional Inspection: Finished steel products are measured and inspected for compliance with specified dimensions and tolerances.

Visual Inspection: Surface quality, such as defects or irregularities, is assessed visually.

Mechanical Testing: Samples of the steel products undergo mechanical tests such as tensile, hardness, and impact testing to verify mechanical properties.

Chemical Analysis: Chemical composition analysis ensures the steel meets specified requirements for alloying elements and impurities.

Non-Destructive Testing: Techniques such as ultrasonic testing, magnetic particle inspection, and radiographic testing may be employed to detect internal defects without damaging the product.

This comprehensive process, from iron ore extraction to the production of sheet metal, involves a series of chemical reactions and physical transformations, each critical to achieving the final product's quality and characteristics.

1.2 Iron-Carbon Diagram:

The iron-carbon diagram, also commonly referred to as the Fe-C phase diagram, stands as a cornerstone in the realm of materials science and metallurgy. As a graphical representation, it serves as a roadmap delineating the intricate dance of phases formed within iron-carbon alloys, elucidating their behavior across varying temperatures and carbon compositions. At its core, this diagram offers a profound understanding of the fundamental principles governing the transformation of steel throughout its heating and cooling cycles, thereby playing a pivotal role in the design, production, and application of steel-based materials.

As iron, the primary constituent of steel, encounters carbon, its steadfast companion in alloying, the resulting amalgamation unveils a spectrum of phases with distinctive properties and behaviors. From the austenite phase, characterized by its high-temperature stability and solid solution of carbon in iron, to the myriad transformations leading to the formation of ferrite, cementite, pearlite, and beyond, the Fe-C diagram intricately maps out the evolution of microstructures as temperature and carbon content fluctuate.

Indeed, the significance of the iron-carbon diagram reverberates across myriad industrial sectors, from construction and automotive engineering to aerospace and beyond. By comprehending the interplay between temperature, carbon content, and resulting phase transformations, engineers and metallurgists can meticulously tailor the properties of steel alloys to suit diverse applications, optimizing strength, hardness, ductility, and other crucial attributes.

In essence, the iron-carbon diagram serves as an indispensable tool, guiding the fabrication processes and material selection endeavors that underpin modern technological advancements. Its elucidation of phase equilibria, solidification pathways, and microstructural evolution stands as a testament to the profound insights gleaned from the marriage of theoretical understanding and empirical observation in the field of metallurgy. Thus, as we embark on an exploration of this diagram's intricacies, we embark on a journey that transcends mere lines and curves, delving into the very essence of steel's transformative journey, from raw material to refined engineering marvel.[1][9][13][14]

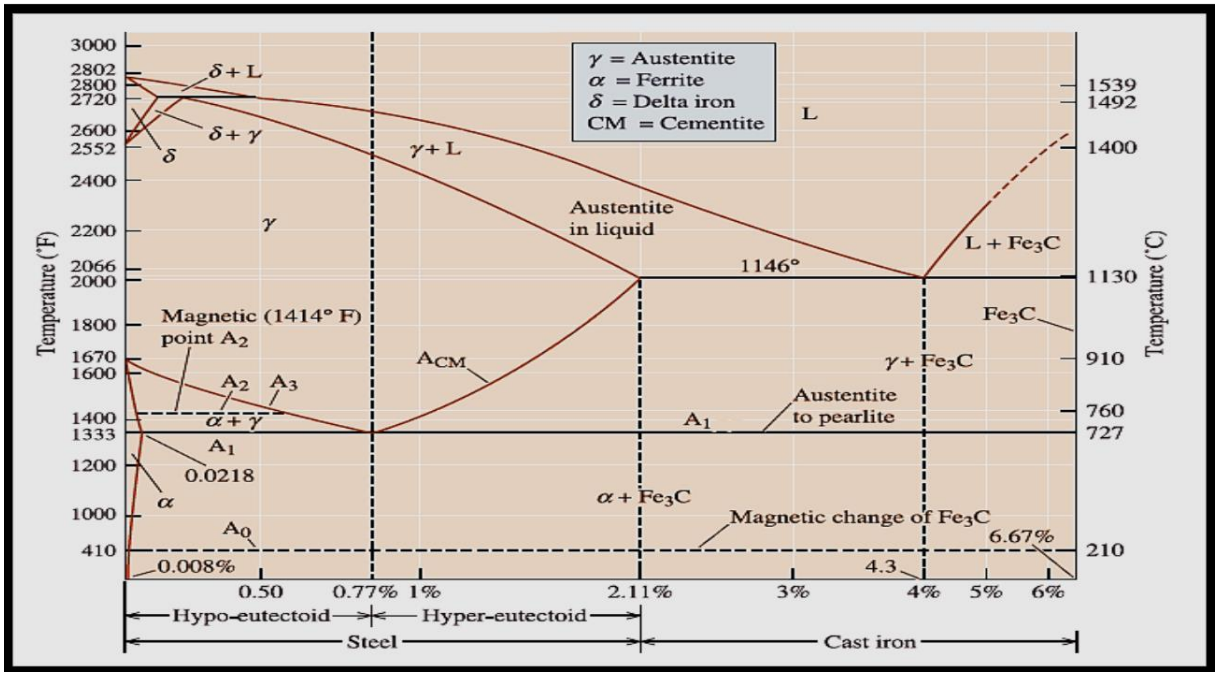

Figure 2. Iron-Carbon Equilibrium Diagram [11]

.

This phase diagram illustrates the phases experienced by Iron-Carbon alloys during cooling to room temperature. Iron-carbon alloys with less than 2% carbon content are commonly referred to as steels, while those exceeding 2% are categorized as cast iron.

1.2.1 Classification of Ferrous Alloys

1. Iron: less than 0.008 wt % C in α-ferrite at room T.

2. Steels: (0.008 - 2.14) wt % C (usually < 1 wt %) α-ferrite + Fe 3 C at room T.

3. Cast Iron: (2.14 - 6.7) wt % (usually < 4.5 wt %).

1.2.2 Phases of iron:

α-Ferrite (Alpha Ferrite):

α-Ferrite is a phase of iron characterized by a body-centered cubic (BCC) crystal structure. It remains stable from room temperature up to approximately 911°C. This phase exhibits a low carbon solubility, with a maximum solubility of around 0.022 wt% at 727°C. α-Ferrite is relatively soft and ductile, making it an important constituent in the microstructure of steel alloys, especially in low carbon steels. Its stability and properties influence the overall mechanical behavior and formability of steel products.[11][13]

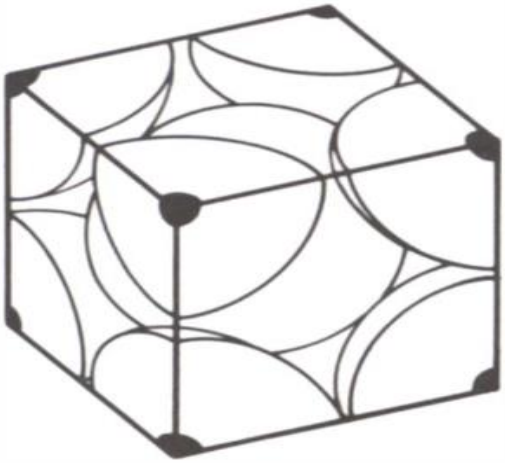

Figure 3. α -Ferrite body-centered cubic crystal structure

γ-Austenite (Gamma Austenite):

γ-Austenite is a phase of iron featuring a face-centered cubic (FCC) crystal structure. It exists within the temperature range of 911°C to 1394°C. This phase has a significantly higher carbon solubility compared to α-ferrite, with a maximum solubility of approximately 2.14 wt% at 1147°C. Austenite is non-magnetic and exhibits greater ductility than ferrite. It serves as the precursor for various microstructural transformations, including the formation of pearlite and martensite upon cooling. Its presence and characteristics profoundly influence the mechanical properties and heat treatment response of steel alloys. [11][13]

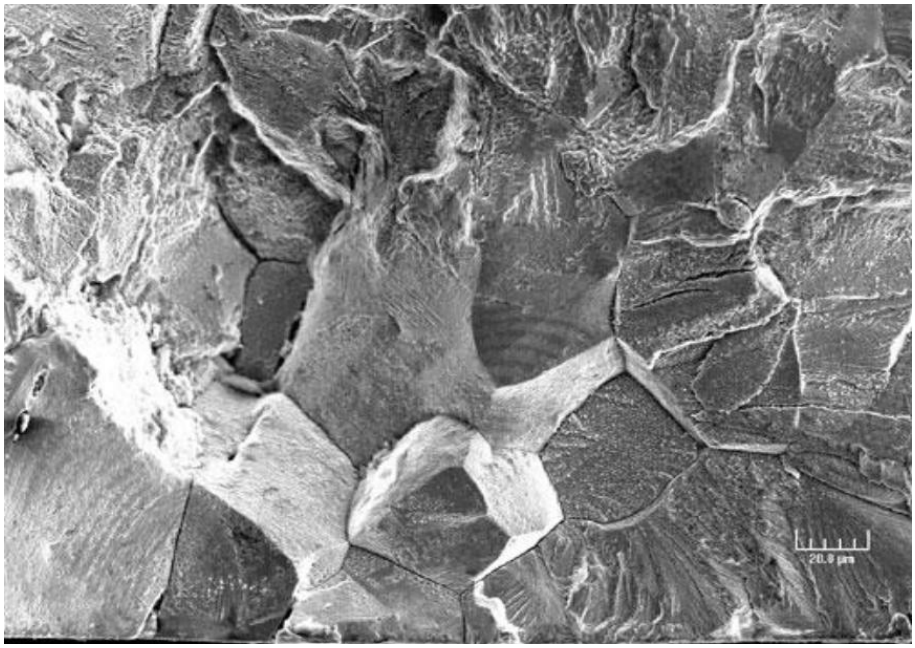

Figure 4. austenite microstructure[32]

δ-Ferrite (Delta Ferrite):

δ-Ferrite is a phase of iron with a body-centered cubic (BCC) crystal structure, similar to α-ferrite but stable at higher temperatures. It exists within the temperature range of 1394°C to the melting point of iron. This phase shares the same structure as α-ferrite but is stable only at elevated temperatures. δ-Ferrite plays a crucial role in the solidification of steel alloys, particularly in high-temperature processes such as casting. Its presence and distribution influence the microstructural homogeneity and mechanical properties of the final product. [11][13]

Cementite Fe3C (Iron Carbide):

Fe3C, commonly known as cementite, is an intermetallic compound composed of iron and carbon. It has a fixed composition with approximately 6.7% carbon. Cementite is a hard and brittle phase that contributes to the strength and hardness of steel alloys. It typically forms as plate-like structures within the microstructure, particularly in pearlite. While cementite remains metastable at room temperature, it can decompose into α-iron and carbon (graphite) when subjected to elevated temperatures within the range of 650 to 700°C. [11][13]

Pearlite

Pearlite is a microstructure that forms in steel through the eutectoid reaction, where austenite transforms into alternating layers of ferrite (a relatively soft and ductile phase) and cementite (a hard and brittle phase). This lamellar structure provides a good balance of strength and ductility. Pearlite forms at the eutectoid temperature of 727°C in both eutectoid and hypoeutectoid steels, and as part of the microstructure in hypereutectoid steels. [11][13]

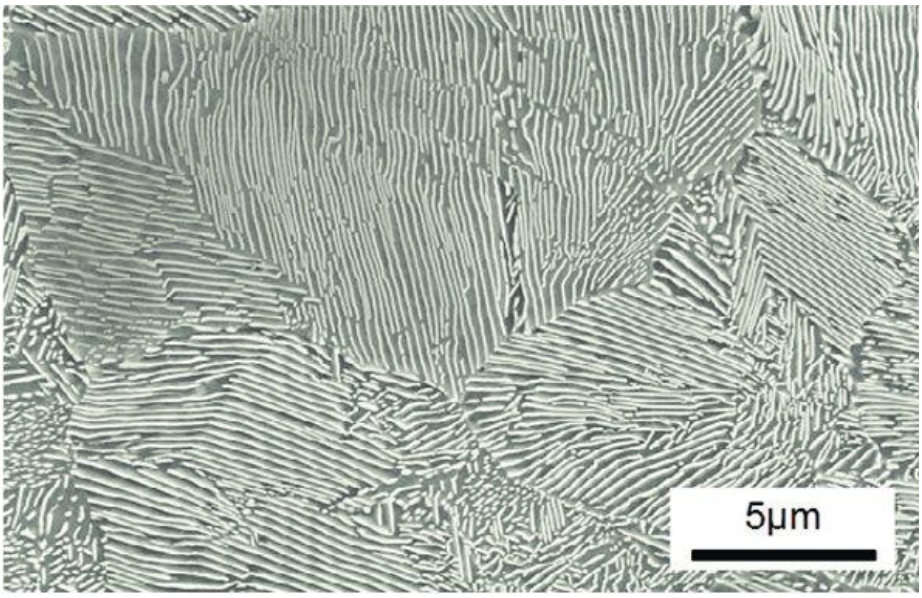

Figure 5. perlite microstructure[33]

Martensite

Martensite is a hard and brittle microstructure formed in steel by a diffusionless transformation from austenite. This transformation occurs when steel is rapidly cooled (quenched) from the austenite phase region to below a critical temperature, leading to a supersaturated solid solution of carbon in a body-centered tetragonal (BCT) crystal structure. Martensite is characterized by its needle-like appearance under the microscope and provides steel with high strength and hardness but low ductility. [11][13]

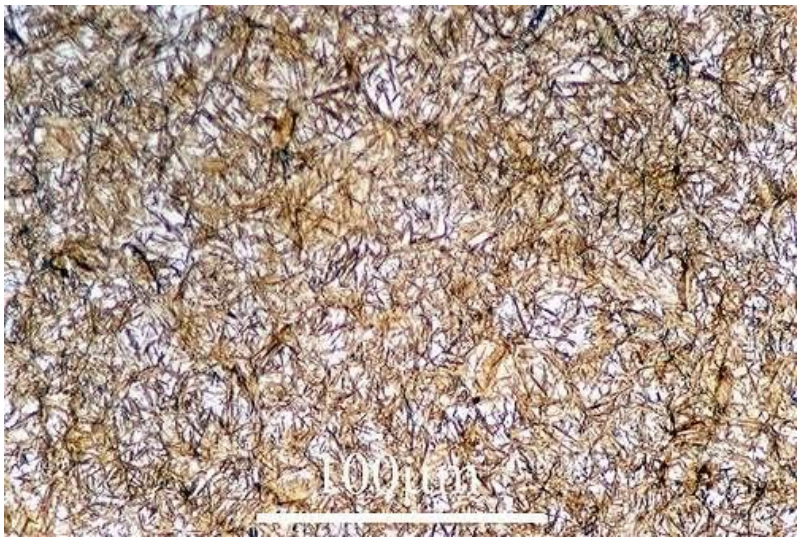

Figure 6. martensite microstructure[34]

Hypoeutectoid Steels

Hypoeutectoid steels are iron-carbon alloys with a carbon content ranging from 0 to 0.83%. These steels consist of primary proeutectoid ferrite and pearlite. The ferrite forms first as the steel cools down from the austenite phase region, followed by the formation of pearlite at lower temperatures. A mixture of ferrite and pearlite characterizes the microstructure of hypoeutectoid steels, with the amount of ferrite exceeding that of pearlite. [13]

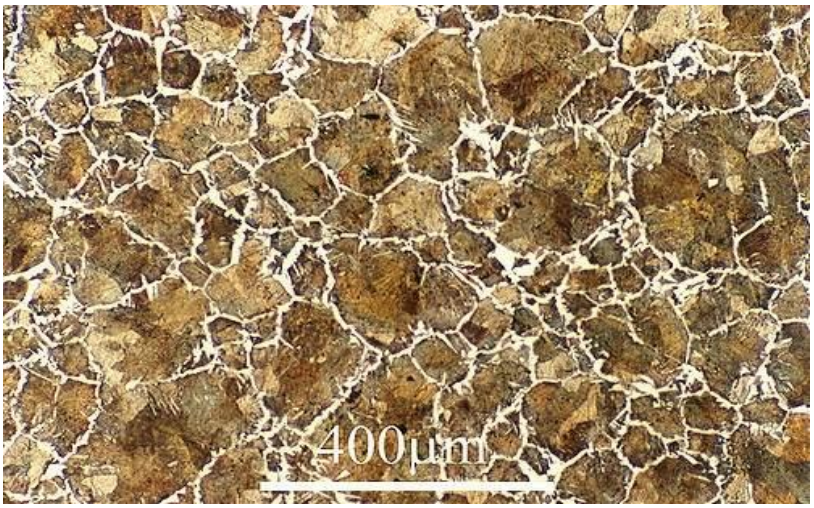

Figure 7. Hypoeutectoid Steel microstructure[35]

Eutectoid Steel

Eutectoid steel is an iron-carbon alloy with a specific carbon content of 0.83%. This composition is at the eutectoid point on the iron-carbon phase diagram. Eutectoid steel entirely consists of pearlite, a microstructure formed by the eutectoid reaction where austenite transforms into a mixture of ferrite and cementite (iron carbide) in alternating layers. This transformation provides eutectoid steel with a balance of strength and ductility.[13]

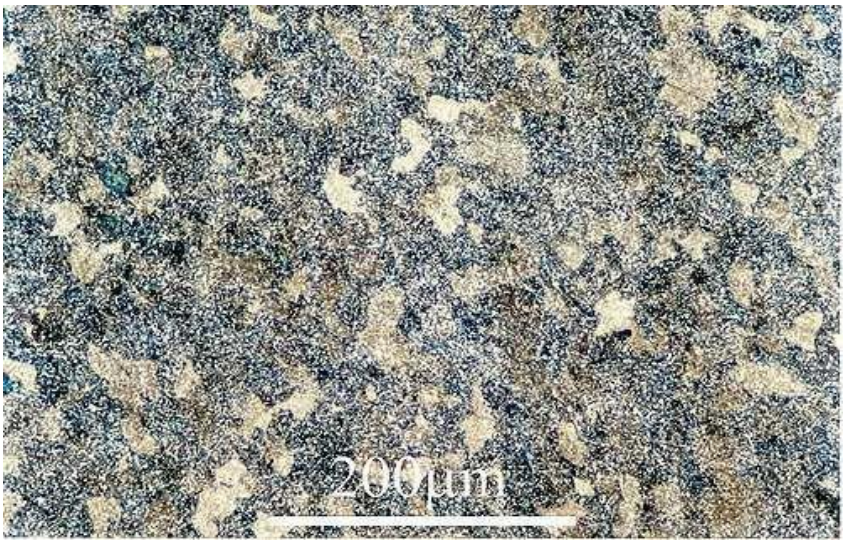

Figure 8. Eutectoid Steel microstructure[36]

Hypereutectoid Steels

Hypereutectoid steels are iron-carbon alloys with a carbon content ranging from 0.83 to 2.06%. These steels consist of primary proeutectoid cementite and pearlite. As the steel cools from the austenite phase region, cementite forms first, followed by the formation of pearlite. A mixture of cementite and pearlite characterizes the microstructure of hypereutectoid steels, with the amount of cementite exceeding that of pearlite.[13]

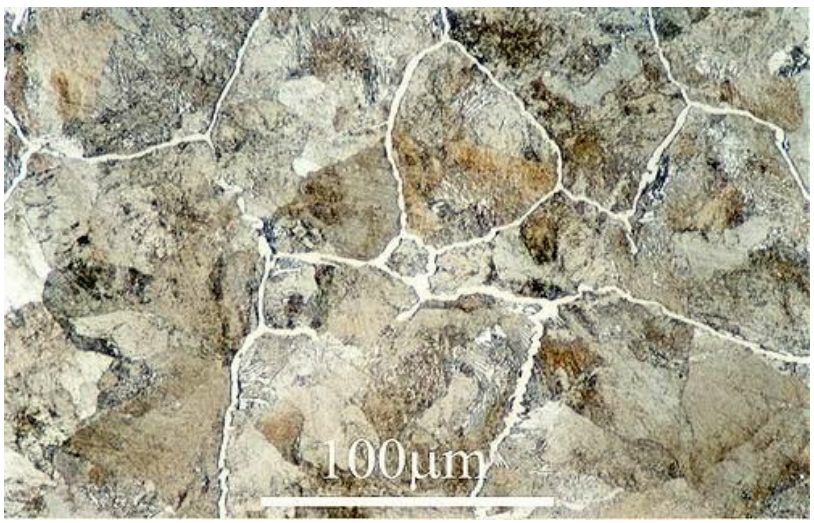

Figure 9. Hypereutectoid Steel microstructure[37]

Fe-C Liquid Solution:

The Fe-C liquid solution refers to the molten state of the iron-carbon system, where carbon atoms are dissolved within the iron matrix. This liquid solution exists above the solidus line in the iron-carbon phase diagram. It plays a vital role during the solidification of steel alloys, facilitating the formation of γ-austenite through peritectic reactions. The composition of the liquid solution varies depending on temperature and carbon content, influencing the subsequent microstructural evolution and properties of the solidified steel. [11][13]

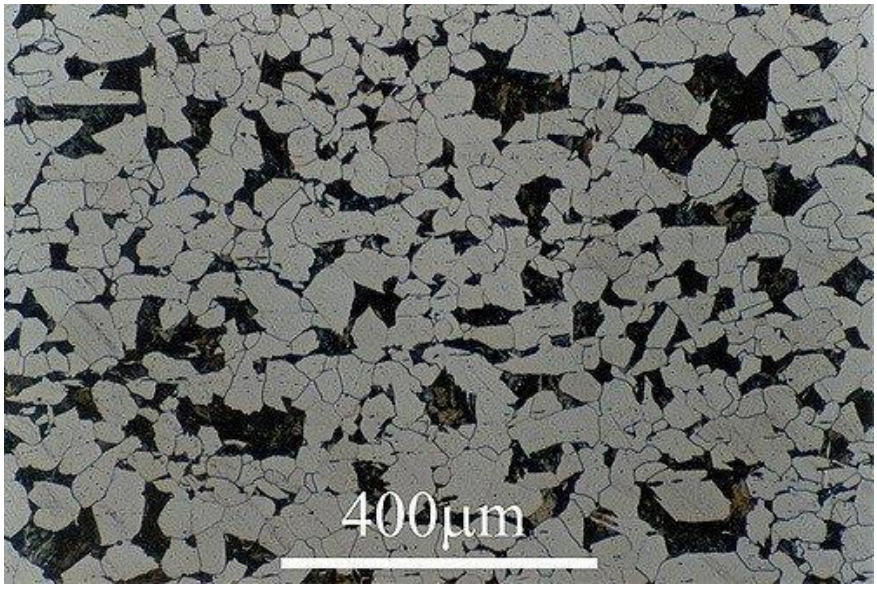

Figure 10. Fe-C Liquid Solution microstructure[38]

1.3 Welding:

1.3.1 Welding definition

Welding, is the process of creating a localized coalescence, where the grain structures of the materials being joined merge together. This coalescence is achieved by heating the materials to the required welding temperatures, with or without the application of pressure, or solely through the application of pressure. The process may also involve the use of filler materials.

The addition of filler material to the joint may be optional, depending on the welding process and the specific requirements of the application. It's worth noting that the term "material" encompasses a broad range of substances, as modern welding techniques can fuse materials beyond metals, including plastic, glass, and ceramics.[15][16]

1.3.2 Types of welding

Welding, as a vital process in fabrication and construction, encompasses a variety of techniques tailored to specific materials, applications, and desired outcomes. These techniques, known as welding types, offer distinct methods for joining materials, each with its unique advantages and considerations.[16]

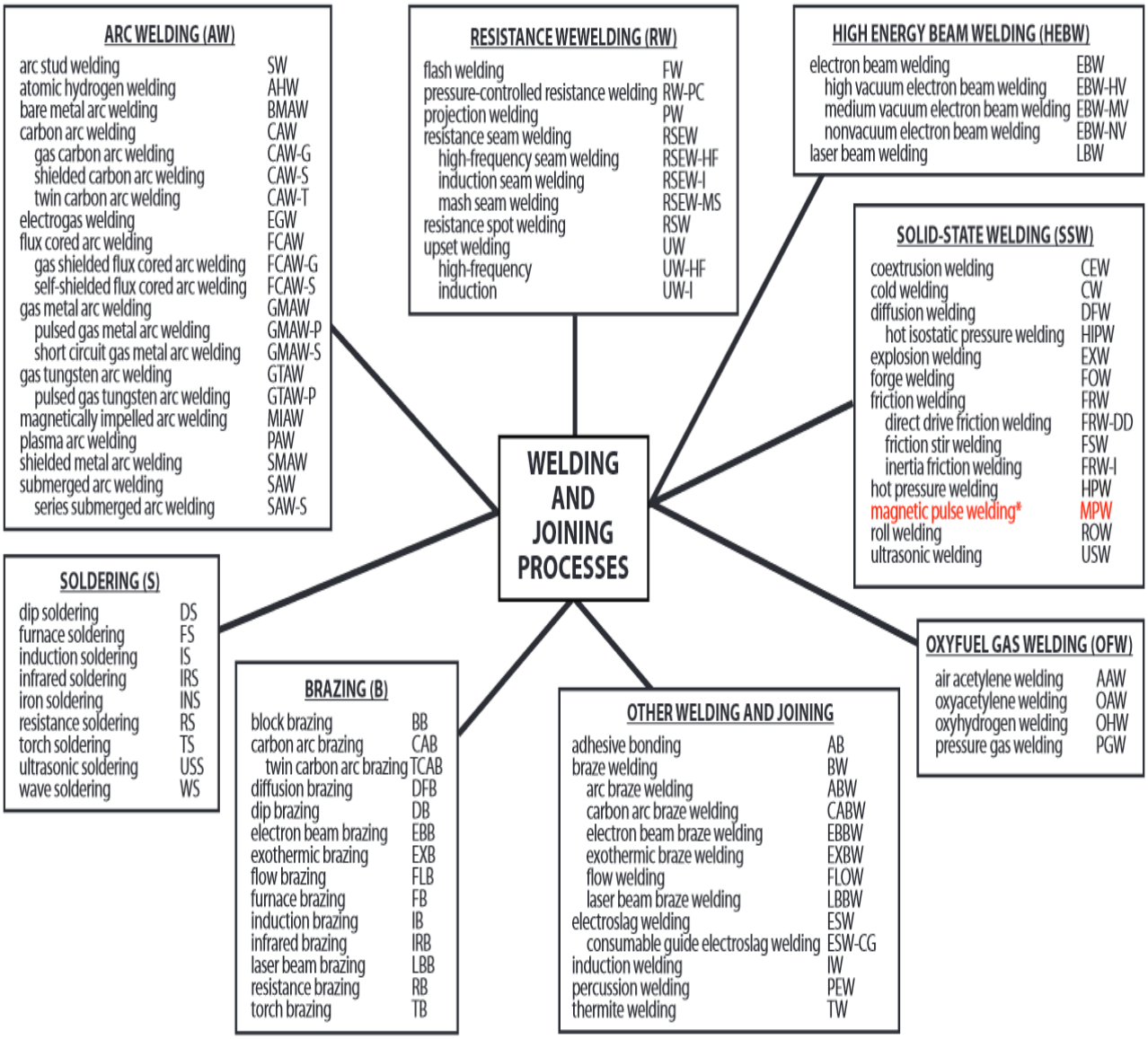

Figure 11. modern welding types[16]

1.3.3 Welding bead

The welding bead refers to the deposited metal that forms the weld joint, resulting from the melting and solidification of the base metal and filler metal (if used)

Understanding the characteristics and properties of the welding bead is crucial, as it directly impacts the strength, integrity, and performance of the welded joint.[15]

Formation of the Welding Bead

The welding arc or heat source melts the base metal and filler metal (if used) to create a molten pool that solidifies into the welding bead

. The shape and size of the welding bead are influenced by factors such as welding parameters (current, voltage, travel speed), joint design, and base metal composition.

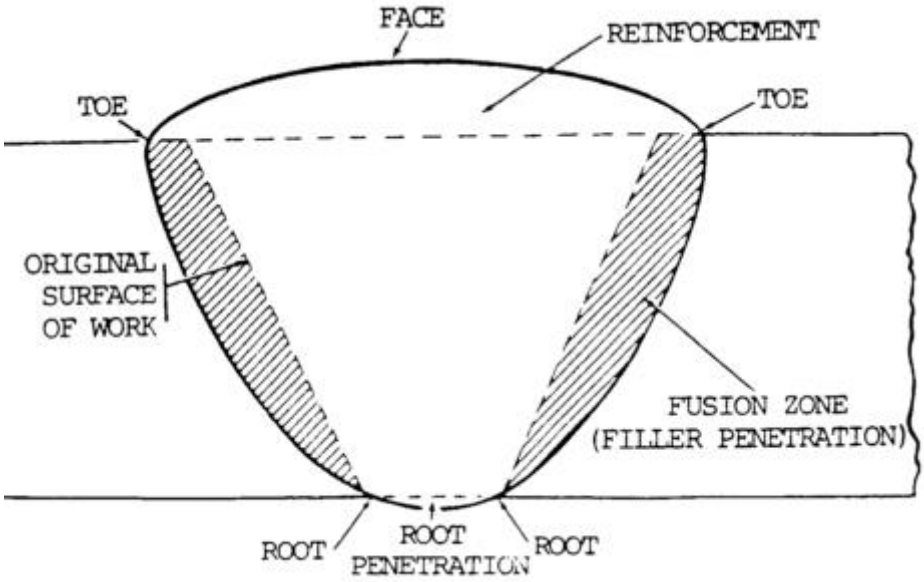

Figure 12. welding bead structure[17]

In the provided diagram, the welding bead is depicted with several key components that are integral to its formation and characteristics. At the top of the weld bead is the Face, which is the exposed surface of the weld on the side from which welding was performed. Surrounding the face is the Reinforcement, which is the extra weld metal that extends beyond the plane of the base metal surface, providing additional strength to the weld. The Toe of the weld is the junction between the face of the weld and the base metal, which is critical for the transition of stress between the weld metal and the base metal. Below the face and reinforcement is the Fusion Zone, also known as the Filler Penetration area, where the filler metal has been deposited and fused with the base metal. The Root refers to the bottom of the weld bead, which is the point at which the backside of the weld intersects with the base metals. Root Penetration is the depth to which the weld metal has penetrated into the joint at the root of the weld.[14][16]

1.3.4 Weldability:

Weldability refers to the capacity of a material to be welded under the fabrication conditions imposed into a specific, suitably designed structure and to perform satisfactorily in the intended service. It encompasses various factors, including the material's ability to undergo the welding

process without cracking or creating other defects, the ease with which a welding procedure can produce a welded joint that meets the required quality standards, and the performance of the welded joint under service conditions.

Weldability is influenced by the material's chemical composition, microstructure, mechanical properties, and thermal conductivity, as well as the welding process parameters such as heat input, welding speed, and the type of filler material used. It also involves considerations of the final welded structure, including the presence of residual stresses, distortion, and the potential for service-related degradation such as corrosion or fatigue.
Weldability assessment encompasses various dimensions crucial for successful welding operations, including operational, metallurgical, and structural factors, each influencing the integrity and performance of welded joints.

Operational Weldability focuses on the practical aspects of welding, assessing the ease of joining materials without defects such as porosity, lack of fusion, or oxide inclusions. Materials like aluminum and magnesium, which form resilient oxide layers, often require specialized welding techniques or surface preparation to achieve satisfactory welds.

Metallurgical Weldability examines the changes in microstructure and material properties resulting from the welding process. The thermal cycle of welding induces various microstructural transformations, influencing the mechanical properties and performance of the welded joint. Key zones include the fusion zone (FZ), where metal melts and solidifies, the bond zone (BZ) at the weld-metal interface, and the heat-affected zone (HAZ), where the base metal undergoes thermal cycling without melting.

Structural Weldability addresses the broader impact of welding on the overall structure, encompassing factors such as residual stresses and susceptibility to cracking. These considerations significantly impact the structural integrity and longevity of welded components, emphasizing the importance of thorough evaluation and mitigation strategies during welding operations.[18]

1.4 SAW welding:

In the early 1930s, the welding industry witnessed a significant breakthrough with the introduction of the Submerged Arc Welding (SAW) process. Pioneering the use of continuous wire electrodes, SAW quickly gained traction, especially during World War II. Over the years, its adoption surged, marked by a steady increase in the yearly tonnage of SAW electrode wire usage. This growth trajectory reflects the expanding embrace of automation and robotic welding

technologies across diverse applications, underscoring SAW's enduring relevance and versatility in modern welding practices.[16]

1.4.1 Definition:

Submerged Arc Welding (SAW) is a fusion welding process renowned for its efficiency and versatility. It entails the creation of a weld by generating intense heat through an electric arc established between the workpiece and a continuously fed filler metal electrode. The arc's heat melts the electrode wire and the base metal, forming a molten weld pool. Crucially, this molten weld pool is shielded from atmospheric contamination by a dense blanket of molten flux and slag. This protective layer, derived from the granular fluxing material preplaced on the workpiece, acts as a barrier, preventing oxidation and impurities from compromising the integrity of the weld. [16] [19]

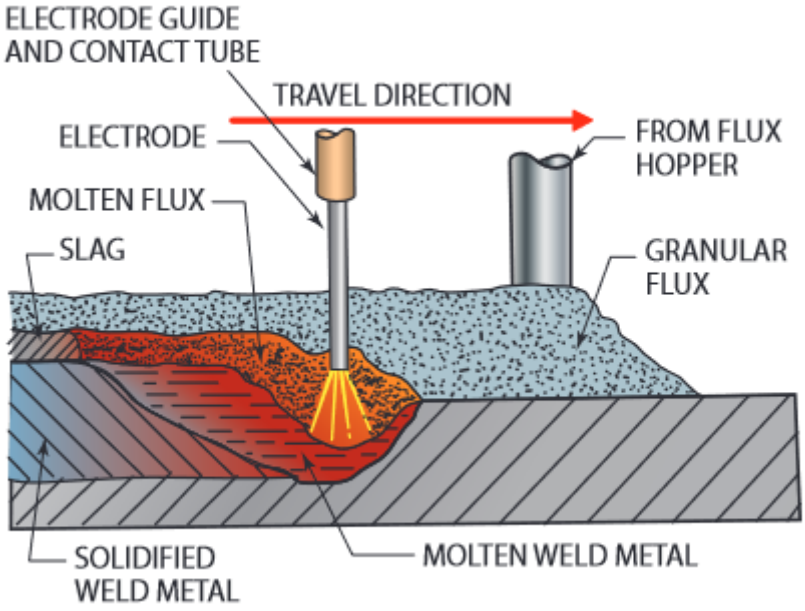

Figure 13. The schematic representation of the Submerged Arc Welding process [16]

1.4.2 The equipment used in SAW:

Submerged Arc Welding (SAW) equipment consists of several key components designed to facilitate the welding process. Here are the main pieces of equipment used in SAW:

Power Source: Provides the necessary electrical current for welding. It can be an AC or DC power source, depending on the welding requirements.

Wire Feeder: Feeds the consumable electrode wire into the welding zone at a controlled rate. The wire feeder ensures a consistent supply of filler material.

Electrode Wire: The consumable electrode wire melts and forms the weld bead. It is typically a solid or cored wire made of a material compatible with the base metals being welded.

Flux Hopper: Stores and dispenses the granular flux, which is used to shield the weld from atmospheric contamination. The flux also stabilizes the arc and contributes to the chemical composition of the weld.

Flux Recovery System: Collects unused flux from the welding area so it can be reused, reducing waste and cost.

Welding Head: Houses the contact tip, where the electrode wire is fed, and the flux nozzle, which directs the flux to the welding zone. The welding head ensures precise delivery of both the wire and the flux.

Travel Mechanism: Moves the welding head along the joint to be welded. This can be a tractor, gantry, or automated system, ensuring consistent weld quality and productivity.

Control System: Manages the parameters of the welding process, including current, voltage, travel speed, and wire feed speed. Modern control systems often incorporate advanced features like feedback loops and pre-programmed welding procedures.

Cooling System: Some SAW setups include cooling systems for the welding head and power source to prevent overheating and ensure continuous operation.

By incorporating these essential welding equipment components into our experimental setup, we aim to achieve precise control, reliable performance, and accurate monitoring throughout the automated SAW process. This enables us to conduct systematic investigations into the effects of current variation on steel welding beads with confidence and precision.

1.4.3 The effect of the welding parameters:

The influence of various submerged arc welding (SAW) parameters on the mechanical properties, macrostructure, and microstructure of welds is profound and scientifically significant..

Arc Voltage: Increasing arc voltage in submerged arc welding leads to changes in the weld pool geometry, which directly affects the macrostructure and microstructure of the weld. A higher arc voltage increases arc length, which subsequently results in a wider but shallower weld bead. This expansion in width and reduction in depth can decrease mechanical strength as the penetration is less deep, leaving less material fused, which is crucial for structural integrity. Furthermore, the enhanced heat input from a higher arc voltage tends to increase the grain size in the weld metal and the heat-affected zone (HAZ), potentially reducing the toughness of the weld due to the coarsening of grains. These transformations in microstructure can detrimentally impact the mechanical properties of the weld, such as its fatigue resistance and tensile strength.[22][24]

Wire Feed Rate: The wire feed rate in SAW significantly influences the deposition rate and consequently the weld's mechanical properties and microstructure. An increased wire feed rate leads to a higher welding current and greater heat input, resulting in increased bead width and penetration. This can enhance the mechanical strength and toughness of the weld if the heat input is controlled effectively. On a microstructural level, a higher deposition rate generally promotes a finer grain structure, provided the cooling rate is adequately managed. This finer grain structure can improve the mechanical properties by enhancing the toughness and ductility of the weld.[26]

Travel Speed: Travel speed is another critical parameter in SAW that affects the weld's characteristics. An increase in travel speed typically reduces the weld bead's width and depth of penetration, which can diminish the mechanical strength due to a smaller volume of material being fused. This reduced penetration can also lead to a smaller HAZ, potentially impacting the weld's overall durability. On the microstructural level, a faster travel speed increases the cooling rate, which refines the grain structure in the weld and HAZ. This refinement can enhance properties such as hardness and yield strength, making the weld more resistant to wear and fatigue.[23]

Current: The current used during SAW directly affects the heat input and energy transferred to the weld pool, impacting both the macrostructure and microstructure. A higher current increases the bead width and depth due to more intense heat generation, improving penetration but potentially compromising toughness if the heat input becomes excessive. The increased heat can also lead to coarser grains in the HAZ and weld metal, adversely affecting the microstructure by reducing toughness and increasing susceptibility to cracking under stress.[23][24]

Electrode Stickout (Welding Wire Extension): Electrode stickout, or the length of the wire that extends from the tip of the contact tube to the workpiece, plays a significant role in determining the resistance heating in the arc. A longer stickout leads to increased resistive heating, which generally results in less intense heating at the weld interface, reducing penetration and potentially altering hardness and strength. This change can affect the macrostructure by leading to shallower penetration and wider bead profiles. On a microstructural level, variations in stickout can affect the fineness of the weld's grains, with shorter stickouts promoting finer grains due to higher heat concentration and more controlled heat input.

Flux: The composition of the flux used in SAW has a significant impact on the welding process and the resulting weld properties. Fluxes can introduce alloying elements such as titanium,

which can enhance mechanical properties by promoting the formation of finer acicular ferrite in the weld metal. The flux also influences slag formation, which controls the fluidity and cooling rate of the weld pool, thereby affecting both the bead shape and size. These changes in flux composition can lead to different microstructures, such as ferritic, martensitic, or bainitic structures, each of which has distinct mechanical properties that can optimize the weld for specific applications.[25][27]

Chapter 2: Materials and experimental techniques

2.1 The studied material:

To conduct this study, we have chosen BS3 grade steel (P265NB) compliant with standard EN 10120, with a material thickness of 3.3 ± 0.13 mm. The steel is commonly used in the gas bottle industry B13, at the company (SNS) Batna.

2.1.1 The chemical composition of the casting analysis:

The chemical composition of the casting analysis of this steel is listed in the following table:

Table 1 The chemical composition of the base metal

Element	C	Si	Mn	P	S	Al	N	Ti
Wt.%	0.15	0.01	0.93	0.015	0.005	0.037	0.004	0.02

2.1.2 Mechanical characterization:

The mechanical characteristics are indicated in the following table:

Table mechanical characteristics

Table 2 mechanical characteristics

Steel	Upper yield strength ReH min MPa	Tensile strength Rm min MPa	Elongation after fracture
P265NB	265	410-500	32

2.2 Filler metal:

In this section, we present the chemical composition of the filler metal EN756-S1, alongside its diameter of 2.4mm. This information serves as a foundational reference point for understanding the composition and characteristics of the filler metal electrode employed in our experimental setup.

Table 3 The chemical composition of the filler metal

Element	C	Si	Mn	P	S	Al	Ni	Cu	Mo
Wt.%	0.061	0.027	0.479	0.006	0.005	0.001	0.047	0.085	0.006

2.3 The flux:

In the Submerged Arc Welding (SAW) process, the flux plays a crucial role in determining the quality of the weld. The flux used in this study is named "SA AR 1 Eliflux" and conforms to the standard EN 14174. Its composition consists of Al_2O_3 (alumina) and TiO_2 (titanium dioxide), which are essential in providing the necessary properties for the welding process, such as protecting the weld pool from atmospheric contamination and stabilizing the arc. The grain size of the flux ranges from 0.2 to 2 mm, ensuring proper coverage and protection during the welding process. The specific composition and grain size distribution of the flux contribute to the mechanical properties and microstructure of the resulting weld.

2.4 Welding Equipment:

In our experimental setup, we utilize a comprehensive array of welding equipment to facilitate precise and controlled Submerged Arc Welding (SAW) processes. This section provides a detailed overview of the key components involved:

2.4.1. Automated Welding Machine NUOVA CMM SW 1.25:

The NUOVA CMM SW 1.25 welding machine serves as the central apparatus for executing the SAW process. It provides the necessary electrical power and control mechanisms to generate the welding arc, regulate current and voltage parameters, and ensure consistent weld bead formation. The process is fully automated, allowing for efficient and repeatable welding operations.

2.4.2. Wire Feeder:

The wire feeder is an integral component that delivers the filler metal electrode (métal d’apport) to the welding arc at a controlled and precise rate. This ensures continuous and uniform deposition of filler metal into the weld pool, maintaining stable welding conditions and quality.

2.4.3. Power Source (Alternating Current):

The power source supplies the electrical energy required to sustain the welding arc. In our experimental setup, an alternating current (AC) power source is employed, offering versatility and adaptability to varying welding conditions and material types.

2.4.4. Welding Station - Lincoln Electric Idealarc® DC600:

The Lincoln Electric Idealarc® DC600 welding station is used to provide a consistent and controlled welding environment. It offers precise control over the welding parameters, such as current and voltage, ensuring optimal welding conditions for each test. This welding station enhances the overall reliability and quality of the welding process.

Figure 14. Welding Equipment (NUOVA CMM SW 1.25 and Lincoln Electric Idealarc® DC600)

By incorporating these essential welding equipment components into our experimental setup, we aim to achieve precise control, reliable performance, and accurate monitoring throughout the automated SAW process. This enables us to conduct systematic investigations into the effects of current variation on steel welding beads with confidence and precision.

2.5 Welding Process:

2.5.1 Sample Preparation:

The preparation of welded samples is a crucial step to ensure consistent and accurate results in subsequent analyses. For this study, a GPL bottle was welded using the Submerged Arc Welding (SAW) process under different welding current settings. The following steps outline the welding process used to create the samples.

2.5.2 Welding Parameters:

The welding parameters were carefully selected and controlled to ensure reproducibility and to investigate the influence of varying electrical currents on the welds. The key parameters included:

- Welding Currents: 280A, 310A, 350A, 390A ±20A

- Voltage: 30V

- Travel Speed: 09mm/s

- Electrode Diameter: 2.4 mm

- Flux Composition: Al_2O_3 + TiO_2

2.5.3 Welding Procedure:

The setup involved calibrating the SW 1.25 welding machine, wire feeder, and Lincoln Electric Idealarc® DC600 to the selected welding parameters. The GPL bottle, made of BS3 grade steel (P265NB), was positioned on the welding table after being cleaned of contaminants. The welding process commenced with the electrode wire being fed through the wire feeder to the welding arc, controlled automatically by the SW 1.25 machine to maintain the chosen current and travel speed. Continuous application of flux covered the welding arc and molten weld pool, preventing oxidation and contamination. Welds were performed longitudinally along the GPL bottle to ensure uniform and consistent weld beads.

After welding, the samples were allowed to cool naturally to room temperature.Once cooled, any remaining flux was removed, and the weld beads were cleaned to prepare them for further analysis.

Figure 15. GPL Bottle with Welded Beads

By following this detailed welding process, we made sure that the samples were consistent and reliable for later mechanical and microstructural tests. This careful approach allowed us to clearly study how different welding currents affect the microstructure and mechanical properties of steel welds.

2.5.4 Sample extraction:

To prepare transverse test samples from welded steel sections while preserving their material properties.

Procedure: Ensure that the equipment is properly set up for cold cutting, avoiding heat generation that could alter the material properties. Position the welded samples for transverse cutting, ensuring that cuts are perpendicular to the weld direction to properly examine the cross-sectional properties of the weld. Execute the cutting process carefully to maintain the integrity of the sample's microstructure. Clean the samples after cutting to remove any debris, ensuring they are ready for further preparation and analysis.

2.6 Metallographic preparation

2.6.1 Sample coating and Polishing

To achieve a smooth, defect-free surface on the samples for detailed microscopic examination.

Materials and Equipment: Polished samples, abrasive papers of varying grit sizes (80, 180, 240, 400, 600, 800, 1000, 1200), felt paper, alumina solution.

Begin by properly coating the samples using cold coating to avoid any structural changes. Start the polishing process with the coarsest abrasive (80 grit) to remove significant surface irregularities and progress sequentially through to the finest grit (1200) to refine the surface. After using each grit size, rotate the sample 90 degrees before moving to the next finer abrasive. This rotation helps to eliminate directional scratches and ensures a uniform surface finish.

Once all abrasive stages are completed, perform the final polishing using felt paper soaked in alumina solution to achieve a high-quality finish. This enhances the smoothness and reflective quality of the sample surfaces, preparing them for detailed microstructural examination.

Figure 16. Metkon Forcipol 1V Grinder/Polisher

2.6.2 Chemical Etching

After polishing, prepare a 2% Nital solution by mixing 2% nitric acid with 98% ethanol. Apply the solution to the polished sample surface for exactly 10 seconds to etch the surface lightly. Immediately after the etching time has elapsed, wash the sample thoroughly with distilled water to remove any residual etching solution and p*revent over-etching. Quickly dry the sample using an air dryer to prevent water spots or oxidation from affecting the surface quality.

This step is crucial for preparing the samples for detailed observation under an optical microscope by highlighting the microstructural details that are not visible on the polished surface alone.

2.7 Macroscopic Examination

Macroscopic examination provides an essential preliminary assessment of the weld quality by revealing surface features and overall integrity of the welded samples. This step is crucial for identifying visible defects and ensuring that the welds meet the required specifications before conducting more detailed microscopic analyses. The examination focuses on evaluating the weld bead's shape, size, and any visible defects such as cracks, porosity, or undercut.

To perform the macroscopic examination, the following tools were used:

Caliper: A precision instrument used to measure the dimensions of the weld bead, including width and height, with high accuracy.

Depth Gauge: An instrument used to measure the depth of features such as undercut and penetration profiles in the weld bead.

These tools were essential in obtaining accurate measurements of the welds and ensuring consistent data collection. Photographs of the caliper and depth gauge used in this examination are provided in Figure

Figure 17. caliper and depth gauge

2.8 Microscopic Examination

Microscopic examination is a vital step in analyzing the detailed microstructural characteristics of the weld metal and the heat-affected zone (HAZ). This examination provides insights into the fine structure of the material, which is critical for understanding the effects of different welding parameters on the weld's mechanical properties.

For this study, an optical microscope Euromex x300 equipped with a DC.1300x camera was utilized. The high-resolution imaging capabilities of this setup allowed for precise visualization of the microstructures. The images were captured and analyzed using the ImageFocus software.

Figure 18. Euromex x300 Optical Microscope with DC.1300x Camera

After polishing the samples to a mirror-like finish and chemically etching them to reveal the microstructure, images of the weld metal zone and the HAZ were captured using the ImageFocus software.

2.9 Microhardness Test

The microhardness test is a method used to determine the hardness of materials on a microscopic scale. This test is particularly useful for measuring the hardness of specific

microstructural features, such as individual phases within a weld or the heat-affected zone (HAZ).

The Vickers hardness test is chosen for this study, it involves pressing a diamond pyramid-shaped indenter with a square base into the material's surface under a specific load. The indenter typically has a face angle of 136 degrees. After the indentation, the diagonals of the resulting impression are measured using a microscope. The procedure includes polishing the sample surface to a mirror-like finish, pressing the diamond indenter into the sample with a 1 kg load for 15 seconds, and then measuring the diagonals of the indentation using a microscope equipped with a scale. The Vickers hardness number (HV) is calculated using the formula:

$$HV = 1.8544.10^3 \frac{F}{d^2}$$

Where F is the applied load in kgf

And d is the average length of the diagonals in millimeters.

The Vickers microhardness test was performed using the FM-810 microhardness tester, this machine offers precise control over the applied load and time, ensuring consistent and accurate measurements.

Figure 19. FM-810 Microhardness Tester

The results from the Vickers microhardness test provide a detailed map of hardness variations within the weld metal and HAZ, which are critical for understanding the material's mechanical properties.

2.10 Tensile Test:

The tensile test is a fundamental mechanical test used to determine a material's tensile strength, yield strength, and elongation properties. During the test, a uniaxial load is applied to a specimen until it fractures, providing valuable insights into the material's behavior under tensile stress. The data obtained from this test include the ultimate tensile strength (Rm), yield strength (Re), and percentage elongation at break (A%).

Ultimate Tensile Strength (Rm):
The ultimate tensile strength is the maximum stress that a material can withstand while being stretched or pulled before breaking. It is calculated using the formula:

$$Rm = \frac{F_{max}}{A_0}$$

Where F_{max} is the maximum load applied
And A_0 is the original cross-sectional area of the specimen.
Yield Strength (Re):
The yield strength is the stress at which a material begins to deform plastically. Prior to the yield point, the material will deform elastically, meaning it will return to its original shape when the applied stress is removed. Yield strength is determined from the stress-strain curve obtained during the test.
Elongation at Break (A %):
Elongation at break is a measure of ductility, representing the extent to which the material can be stretched before breaking. It is expressed as a percentage of the original gauge length of the specimen:

$$A\% = \frac{L_f - L_0}{L_0} \times 100$$

where L_f is the final length of the specimen after fracture
And L_0 is the original gauge length.
The tensile test samples were prepared according to the European Standard NF EN 1442. Four specimens, each with a length of 170 mm and a width of 25 mm, were extracted from each weld configuration in the transverse direction to the weld seam. This standard ensures that the test samples are consistent and that the results are comparable.

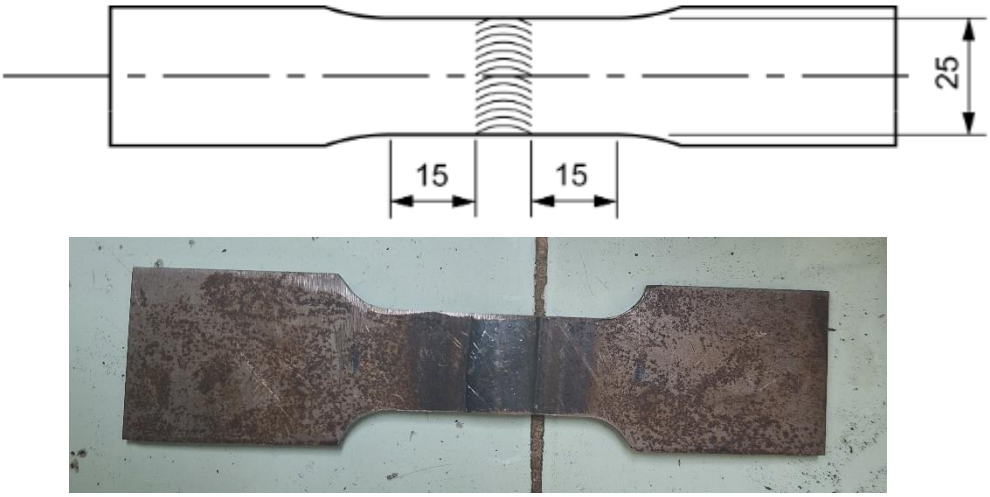

Figure 20. tesile specimen

The tensile tests were conducted using the Zwick/Roell BT1-EXMACRO.1BL tensile testing machine. The machine applied a uniaxial load to the specimens until failure, measuring the force and the elongation during the test. The TestExpert software was used to record and analyze the results, providing detailed data on tensile strength, yield strength, and elongation at break.

Figure 21. Zwick/Roell BT1-EXMACRO.1BL Tensile Testing Machine

The results from these tests are critical for understanding the mechanical properties of the welds and how different welding parameters affect these properties.

2.11 Scanning Electron Microscopy (SEM) and Energy Dispersive X-ray Spectroscopy (EDS)

Scanning Electron Microscopy (SEM) is a powerful technique used to observe the surface morphology and microstructural features of materials at high magnifications. SEM operates by focusing a beam of electrons onto the sample surface. These electrons interact with the atoms in the sample, producing various signals that can be detected and converted into high-resolution images. Secondary electrons emitted from the sample surface provide detailed topographical information, while backscattered electrons offer compositional contrast based on atomic number differences.

Energy Dispersive Spectroscopy (EDS) is often coupled with SEM to provide elemental analysis. When the electron beam hits the sample, it can eject inner-shell electrons from the atoms. The vacancies left by these ejected electrons are filled by electrons from higher energy levels, and this transition releases characteristic X-rays. By detecting these X-rays, EDS can identify the elements present in the sample and determine their relative concentrations.

For SEM and EDS analyses, the samples were meticulously prepared to ensure optimal imaging and analysis quality. The samples were polished using abrasive papers of varying grit sizes, starting from coarse (80 grit) and progressing to very fine (3000 grit). After the initial polishing, the samples were further polished using an alumina solution to achieve a mirror-like finish, which is crucial for obtaining high-resolution images. Before placing them in the SEM, the samples were washed with ethanol to remove any contaminants, ensuring a clean surface for analysis.

For this study, the SEM and EDS analyses were performed using the JCM-7000NeoScope™ Benchtop SEM. This high-resolution SEM is equipped with an integrated EDS detector for elemental analysis.[30]

Figure 22. JCM-7000NeoScope™ Benchtop SEM with EDS Detector

2.12 X-ray Diffraction (XRD) Test:

X-ray Diffraction (XRD) is a powerful analytical technique used to identify the crystalline phases present in a material and to determine its crystallographic structure. XRD works by directing X-rays at a sample and measuring the angles and intensities of the X-rays that are diffracted by the sample's crystal lattice. This technique provides detailed information about the atomic arrangement within the material, which is crucial for understanding its properties and behavior.

The fundamental principle underlying XRD is Bragg's Law, which relates the wavelength of the X-rays to the angle at which they are diffracted and the distance between the planes in the crystal lattice. Bragg's Law is expressed mathematically as:

$$n\gamma = 2dsin\theta$$

where:

n is the order of reflection (an integer),

γ is the wavelength of the X-rays,

d is the distance between the crystal planes, and

θ is the angle of incidence at which diffraction occurs.

This equation shows that diffraction occurs when the path difference between rays scattered by adjacent planes is an integer multiple of the wavelength. By measuring the angles θ at which diffraction peaks occur and knowing the wavelength γ, the interplanar spacing d can be calculated.

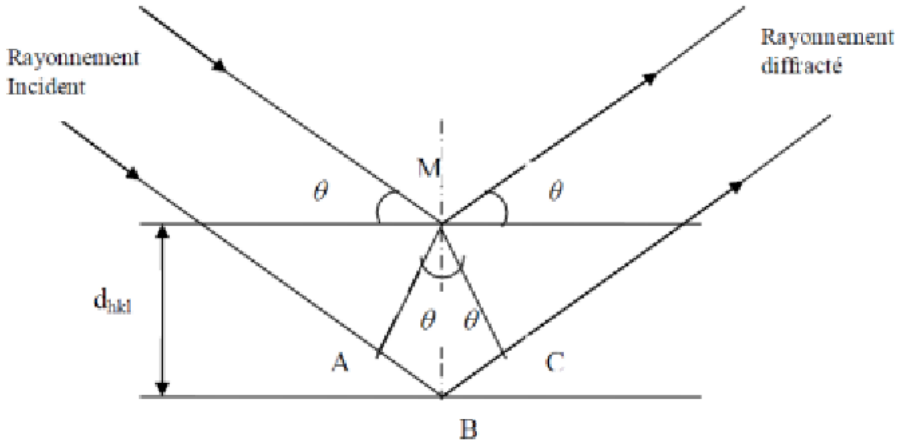

Figure 23. Illustration of Bragg's Law

For XRD analysis, the samples were prepared to ensure accurate and reliable results. The samples were polished to a smooth finish using abrasive papers and diamond paste, similar to the SEM preparation process. This was necessary to produce a flat and even surface for optimal X-ray diffraction. Before analysis, the samples were washed with ethanol to remove any contaminants, ensuring a clean surface for accurate results.

The XRD analysis was performed using the Rigaku Miniflex600 X-ray diffractometer. This advanced instrument is capable of precise angle measurements and high-resolution diffraction patterns, providing comprehensive data on the crystalline phases and structural properties of the welded samples.[28]

Figure 24. Rigaku Miniflex600 X-ray Diffractometer

Chapter 3:Results and discussion

3.1 Macroscopic Examination

The macroscopic examination involved measuring the weld zone width, the heat-affected zone (HAZ) width, and the depth of the welds for samples produced at different welding currents. These measurements provide initial insights into how varying electrical currents influence the overall geometry and extent of thermal effects on the welds.

In this study, macroscopic examination was performed using a caliper and depth gauge to measure the width of the weld zone, the width of the HAZ, and the depth of the weld.

The following tables summarize the measurements for each parameter at different welding currents. Each measurement was taken at ten different locations on each sample to ensure accuracy and consistency.

Table 4: Weld Zone Width (in mm)

Amperage	1	2	3	4	5	6	7	8	9	10	Average
280A	12,45	13,2	12,3	12,7	12,85	13,1	12,55	12,8	12,9	13,05	12,89
310A	14,1	13,55	14,65	14,1	14,2	13,75	14,05	14,35	14,15	13,9	14,12
350A	16,1	16,5	16,6	16,4	16,3	16,45	16,55	16,6	16,35	16,5	16,48
390A	17,65	17,3	17,25	17,4	17,5	17,55	17,35	17,45	17,6	17,4	17,43

Table 5: Heat-Affected Zone (in mm)

Amperage	1	2	3	4	5	6	7	8	9	10	Average
280A	29,35	30,5	31,2	30,15	30,75	30,45	30,6	31,05	30,9	30,85	30,58
310A	31,95	35,55	36	34,2	33,15	34,05	33,75	34,5	33,9	34,35	34,73
350A	38,55	36,5	39,45	38,2	37,8	38,35	37,55	38,1	37,95	37,65	38,14
390A	52,15	58,9	55,85	55,6	56,75	57,2	54,8	56,3	57,6	56,1	56,42

Table 6: Depth of Weld Zone (in mm)

Amperage	1	2	3	4	5	6	7	8	9	10	Average
280A	0,86	1,28	1,18	1,03	1,15	1,1	1,2	1,23	1,08	1,12	1,13
310A	1,12	1,44	1,3	1,29	1,37	1,35	1,22	1,32	1,4	1,25	1,34
350A	1,45	1,59	1,22	1,42	1,33	1,48	1,39	1,36	1,53	1,4	1,42
390A	1,61	1,75	1,8	1,68	1,7	1,73	1,65	1,72	1,77	1,66	1,71

The following graphs provide a visual comparison of the measurements for each parameter at different welding currents. The x-axis represents the measurement number, and the y-axis represents the measured value in millimeters. Each line corresponds to a different welding current.

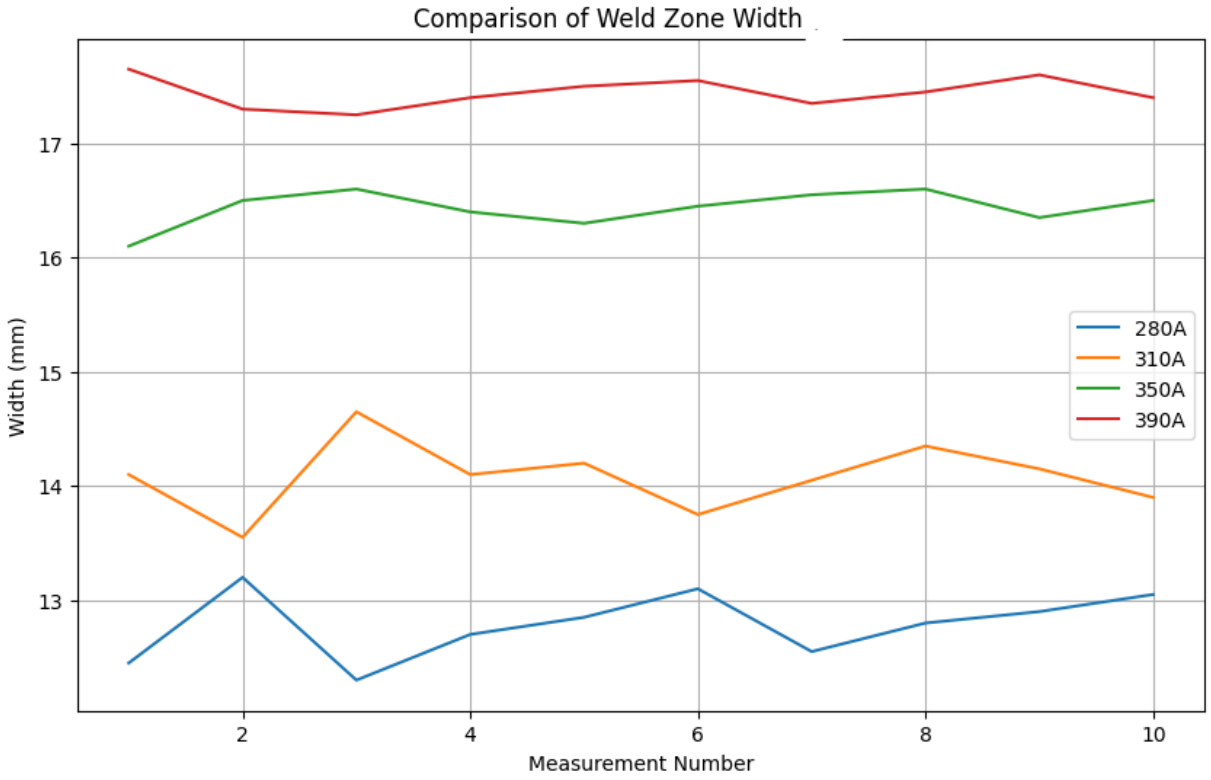

Figure 25. Comparison of Weld Zone Width

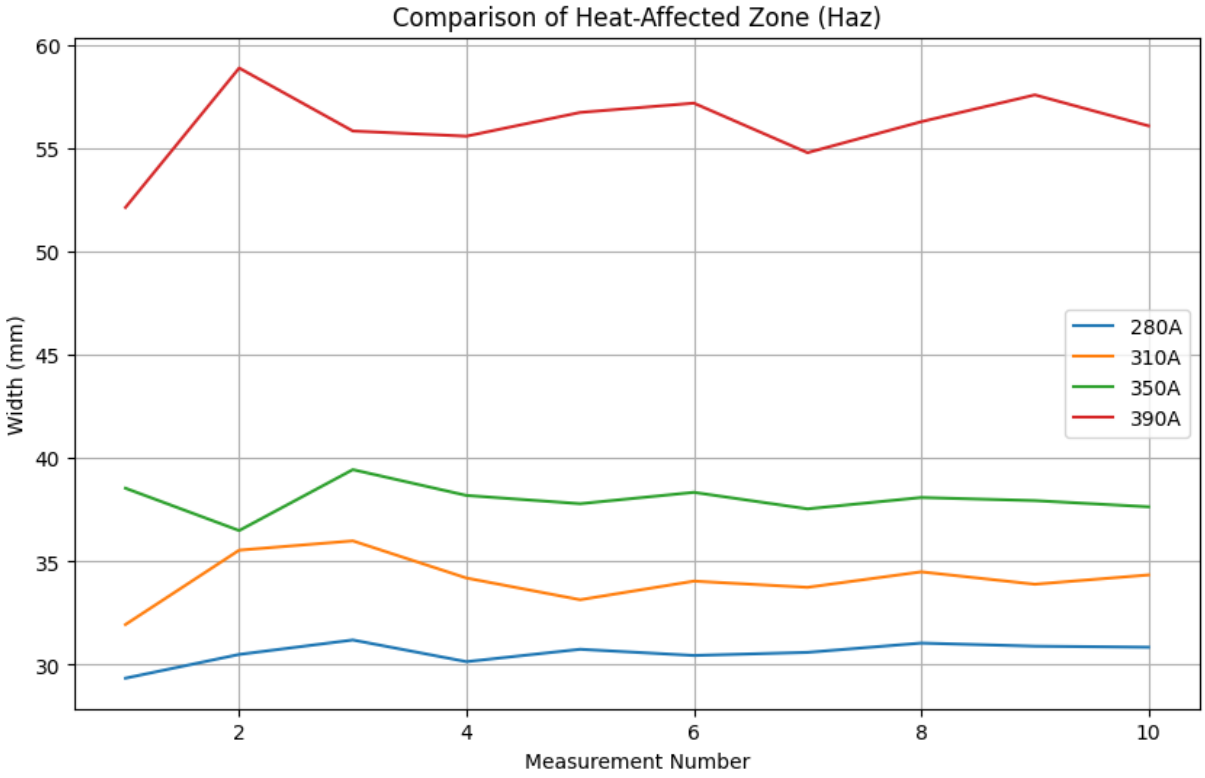

Figure 26. Comparison of Heat-Affected Zone (Haz)

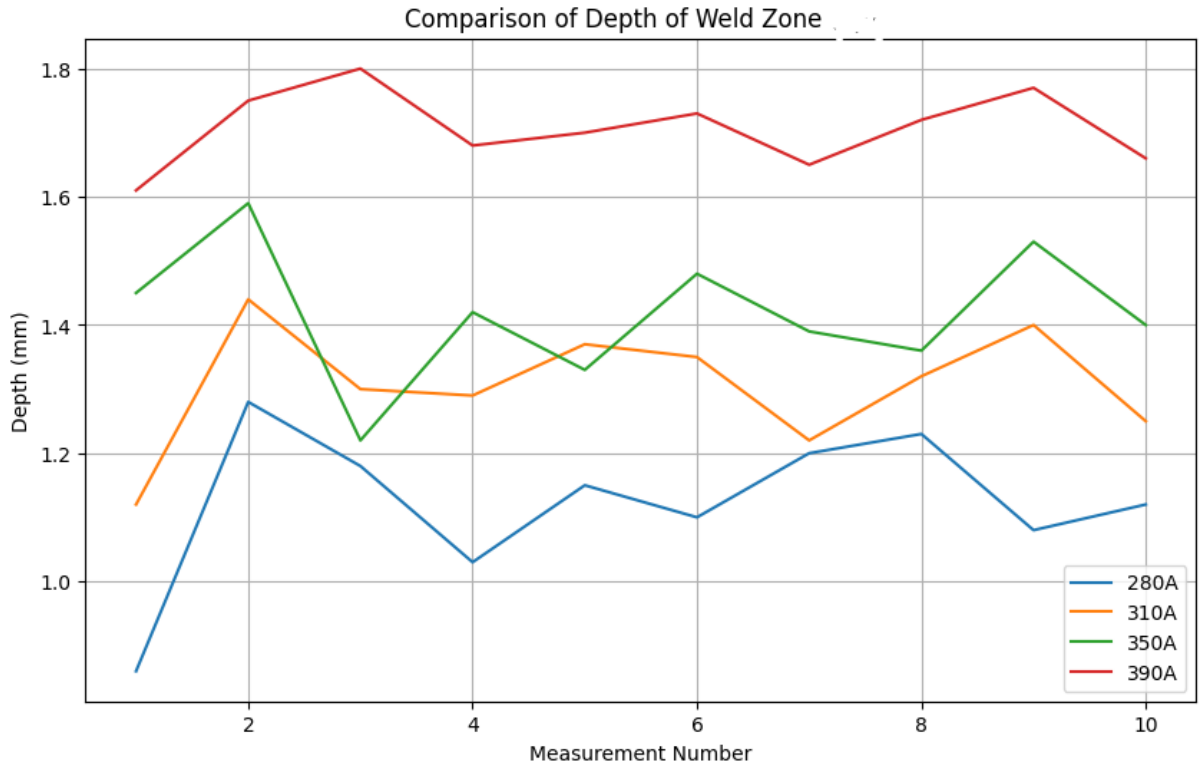

Figure 27. Comparison of Depth of Weld Zone

During the macroscopic examination, the following observations were made:

Weld Zone Width: The width of the weld zone increased with increasing current. At 280A, the welds were narrower, whereas at 390A, the welds were significantly wider.

Heat-Affected Zone (HAZ): Similarly, the HAZ width increased with higher currents. The HAZ was more pronounced at higher currents, indicating more significant thermal effects.

Depth of Weld: The depth of the weld increased with increasing current, showing deeper penetration at higher currents.

Visible Defects: No visible defects such as cracks or porosity were observed in any of the samples. The weld beads appeared uniform and consistent across all currents.

The macroscopic examination of the welded samples revealed distinct differences in weld bead geometry and overall weld quality as the welding current increased from 270A to 390A. At lower currents, the weld bead exhibited a smoother and more uniform appearance, with minimal porosity and defects. As the current increased, the weld beads became wider and showed signs of increased heat input, such as larger heat-affected zones (HAZ) and more pronounced grain growth. These observations are consistent with the literature, which indicates that higher welding currents lead to greater heat input, resulting in wider weld beads and more significant thermal effects on the surrounding material. The increased heat input promotes grain coarsening and a more extensive HAZ, primarily due to the thermal cycles associated with different welding currents. These findings underscore the critical balance between welding parameters and their impact on both the macroscopic and microscopic characteristics of welds, highlighting the importance of optimizing welding conditions to achieve desired weld qualities.

3.2 Microscopic exam

The microscopic examination was conducted to analyze the microstructure of the base metal, weld zone, and heat-affected zone (HAZ) for samples welded at different currents (280A, 310A, 350A, 390A). The samples were polished to a mirror-like finish and chemically etched using a 2% Nital solution to reveal the microstructural features.

An optical microscope Euromex x300 with a DC.1300x camera was used to capture images of the microstructure. The images were taken at 400x magnification to provide detailed views of the microstructural changes induced by welding. The samples were examined under the microscope, and images of the base metal, weld zone, and HAZ were captured for each welding current.

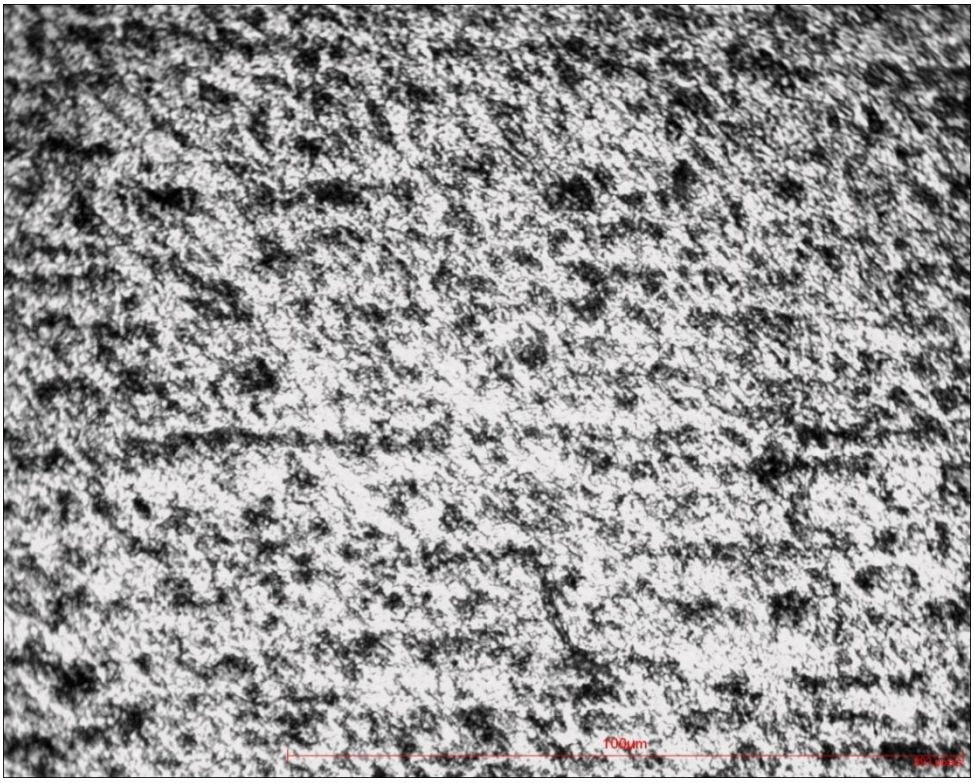

Figure 28. Base Metal Microstructure (400x)

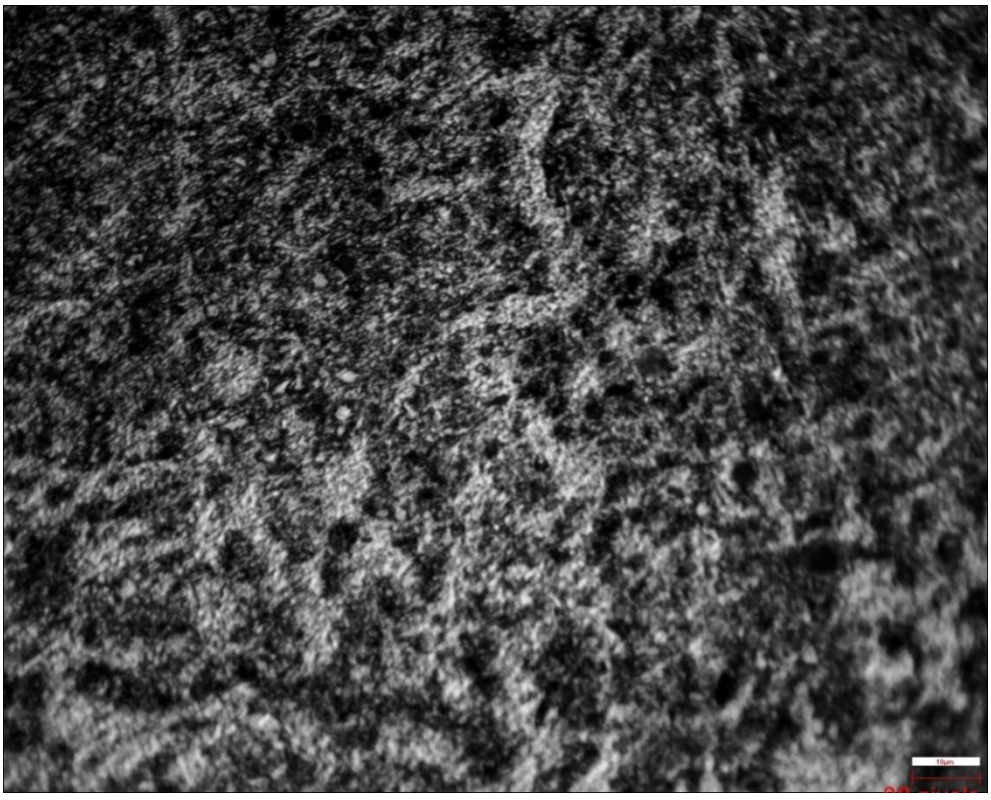

Figure 29. 280A Weld Zone Microstructure

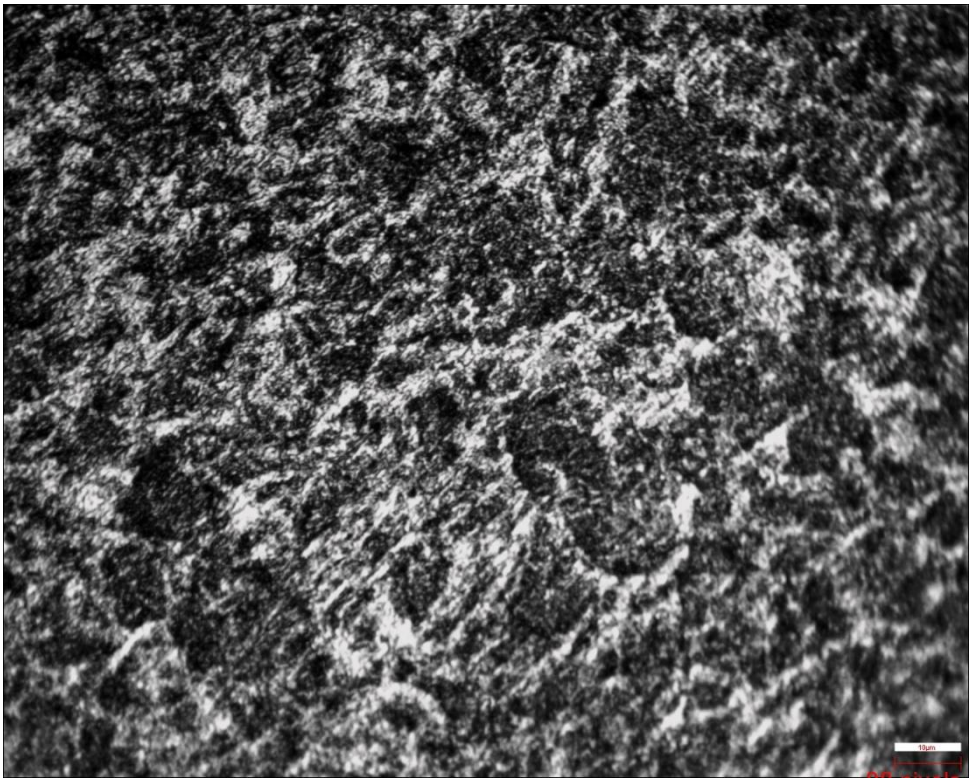

Figure 30. 280A HAZ Microstructure

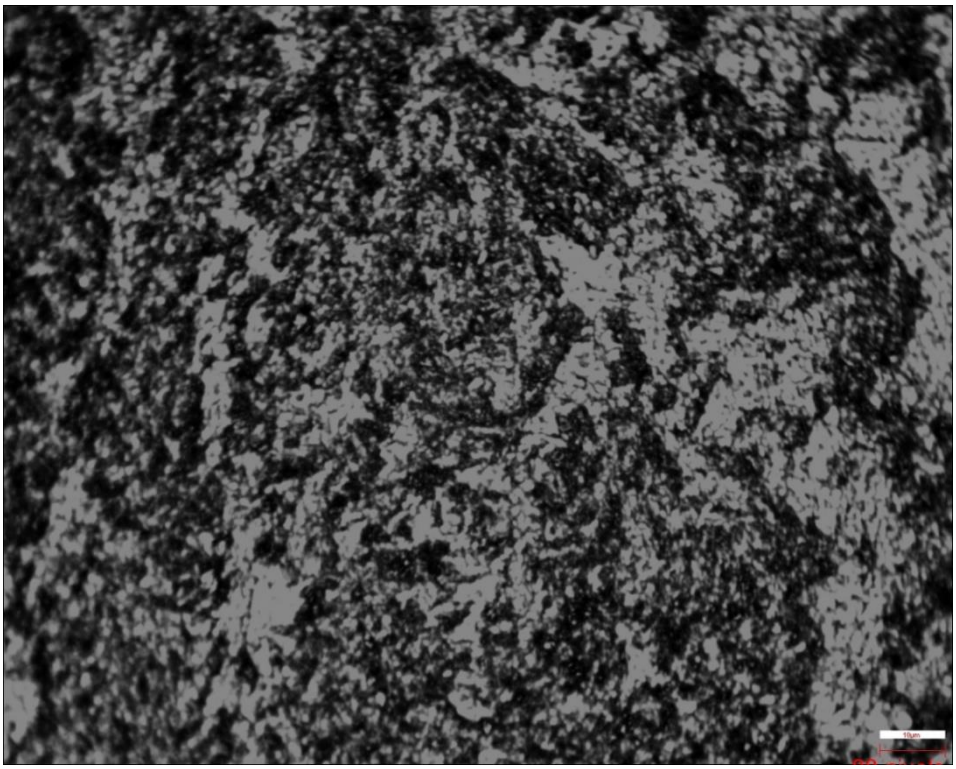

Figure 31. 310A Weld Zone Microstructure

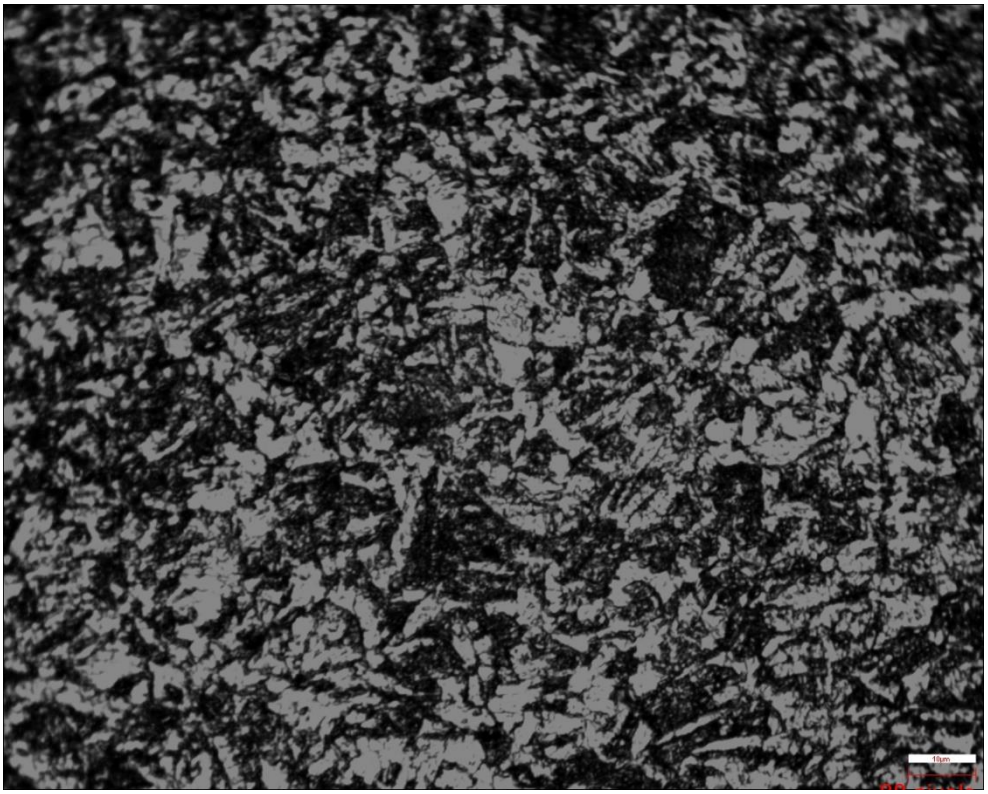

Figure 32. 310A HAZ Microstructure

Figure 33. 350A Weld Zone Microstructure

Figure 34. 350A HAZ Microstructure

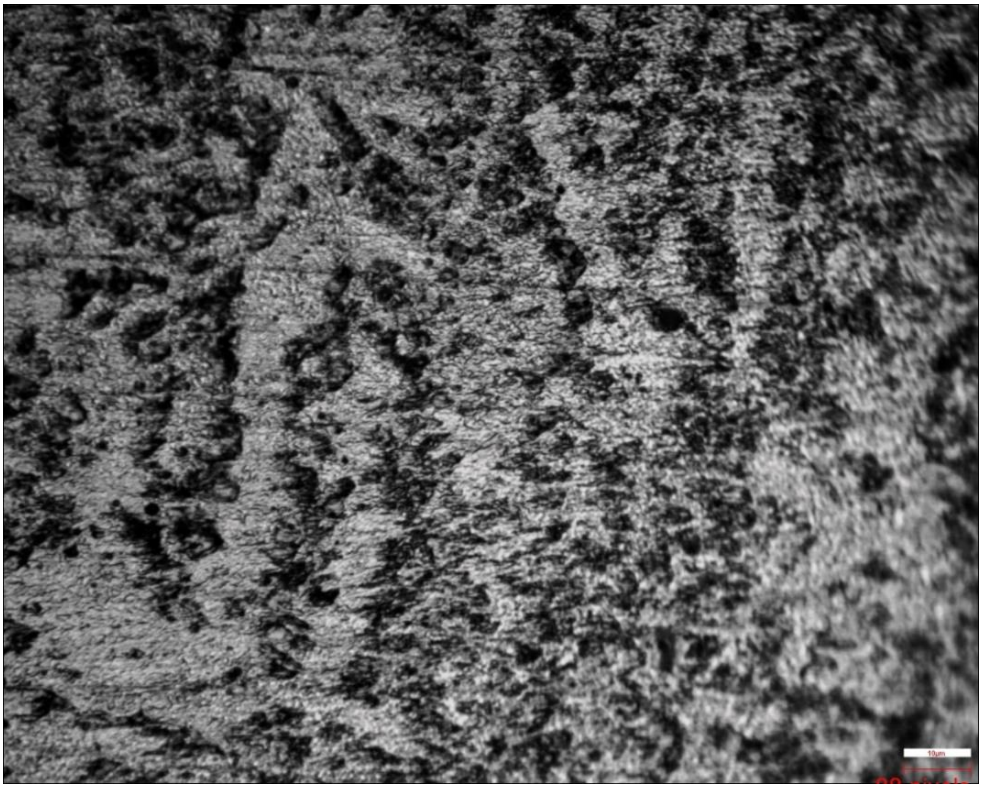

Figure 35. 390A Weld Zone Microstructure

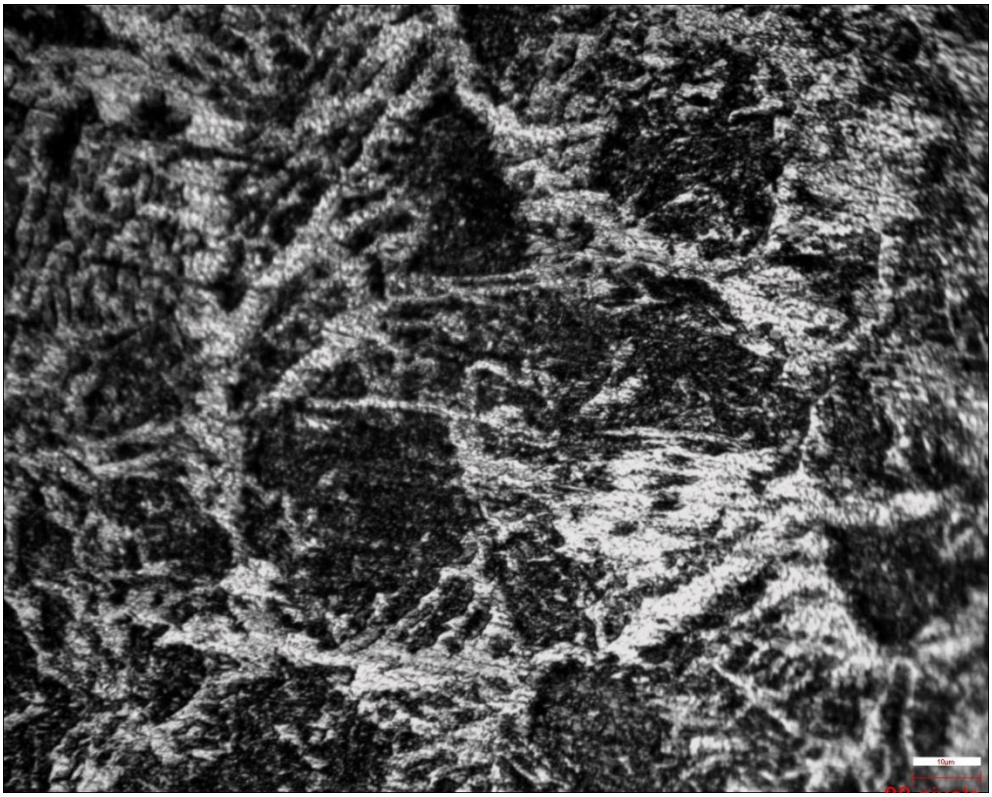

Figure 36. 390A HAZ Microstructure

The microstructure of the base metal is characterized by the presence of ferrite and pearlite. Ferrite appears as light regions under the microscope, while pearlite appears as alternating dark and light bands. This distribution and morphology of ferrite and pearlite are typical of a rolled sheet, where the grains are elongated and oriented due to the rolling process. As the welding current increases, the portion of ferrite in the weld zone also increases. At 280A, the microstructure predominantly features proeutectoid ferrite and acicular ferrite. As the electrical current increases to 310A, the presence of acicular ferrite remains significant, with the introduction of Widmanstätten ferrite, indicating a shift towards a more plate-like structure. At 350A, the microstructure shows a mix of acicular ferrite, Widmanstätten ferrite, and the emergence of allotriomorphic ferrite along grain boundaries, suggesting a variation in cooling rates within the weld zone. Finally, at 390A, the dominance of acicular ferrite decreases, with Widmanstätten ferrite and grain boundary ferrite becoming more prominent. This progression shows that by increasing the welding current, the portion of ferrite in the weld zone increases, reflecting the changes in thermal cycles and cooling rates induced by higher electrical currents.

As the welding current increases, the grains in the HAZ become coarser, and the composition of ferrite types evolves significantly. At 280A, the HAZ predominantly features polygonal ferrite and acicular ferrite, contributing to a balance of microstructural toughness. As the electrical current increases to 310A, the presence of acicular ferrite remains significant, with

polygonal ferrite still being present. At 350A, the microstructure shows a mix of acicular ferrite, polygonal ferrite, and the emergence of Widmanstätten ferrite and allotriomorphic ferrite along grain boundaries, indicating a variation in cooling rates within the HAZ. Finally, at 390A, the dominance of acicular ferrite increases further, with a significant presence of Widmanstätten ferrite and allotriomorphic ferrite, reflecting the higher cooling rates and more complex thermal cycles. This progression shows that by increasing the welding current, the portion and types of ferrite in the HAZ become more diverse and pronounced, reflecting the change.

3.3 SEM exam:

The Scanning Electron Microscope (SEM) analysis provides detailed insights into the microstructural features of the weld zone. The SEM used for this study was a Tescan Vega3, and the samples were examined at a magnification of 350x. Samples were prepared by polishing with abrasives up to 3000 grit and finished with diamond paste to achieve a mirror-like surface, ensuring optimal resolution in the SEM images. The samples were then chemically etched to reveal the microstructure and cleaned with ethanol to remove any contaminants.

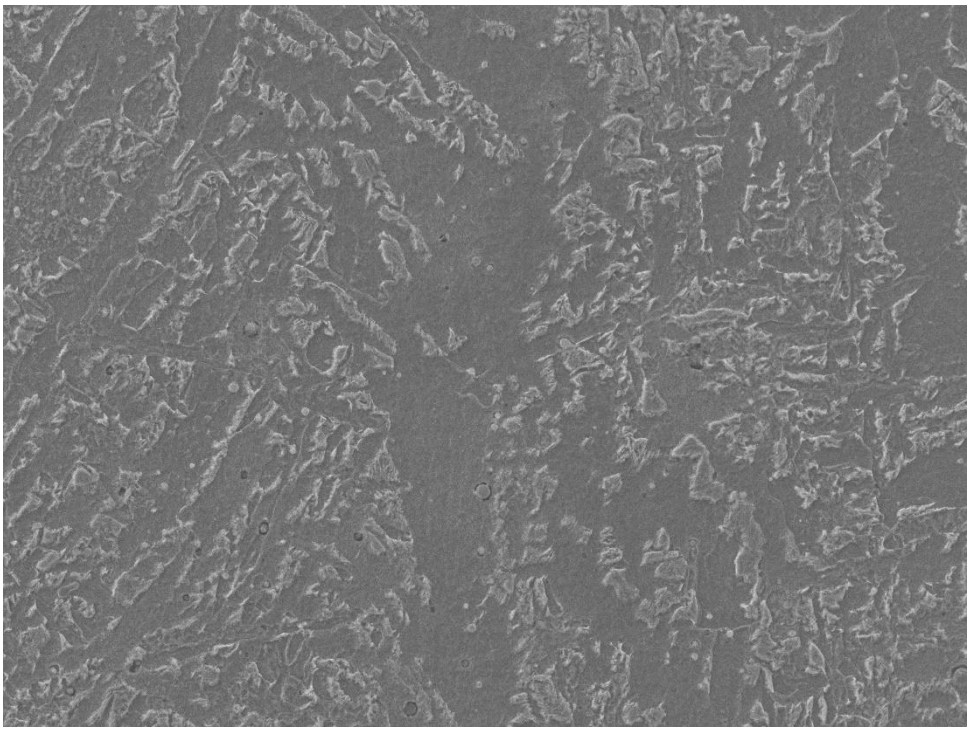

Figure 37. 280A WZ SEM Image at 350x Magnification

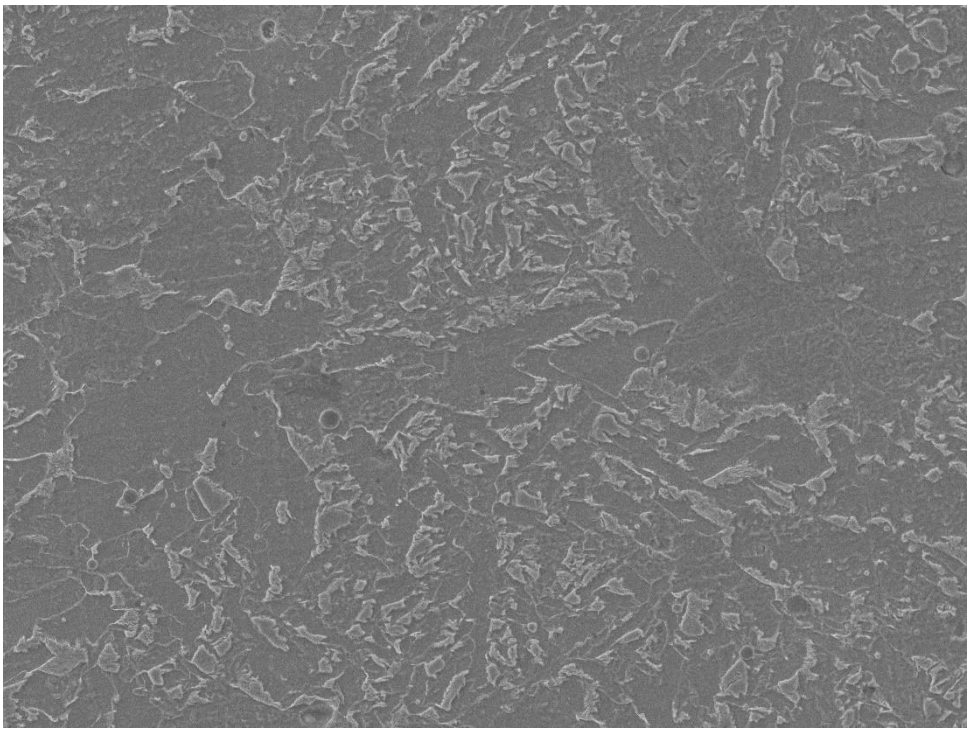

Figure 38. 310A WZ SEM Image at 350x Magnification

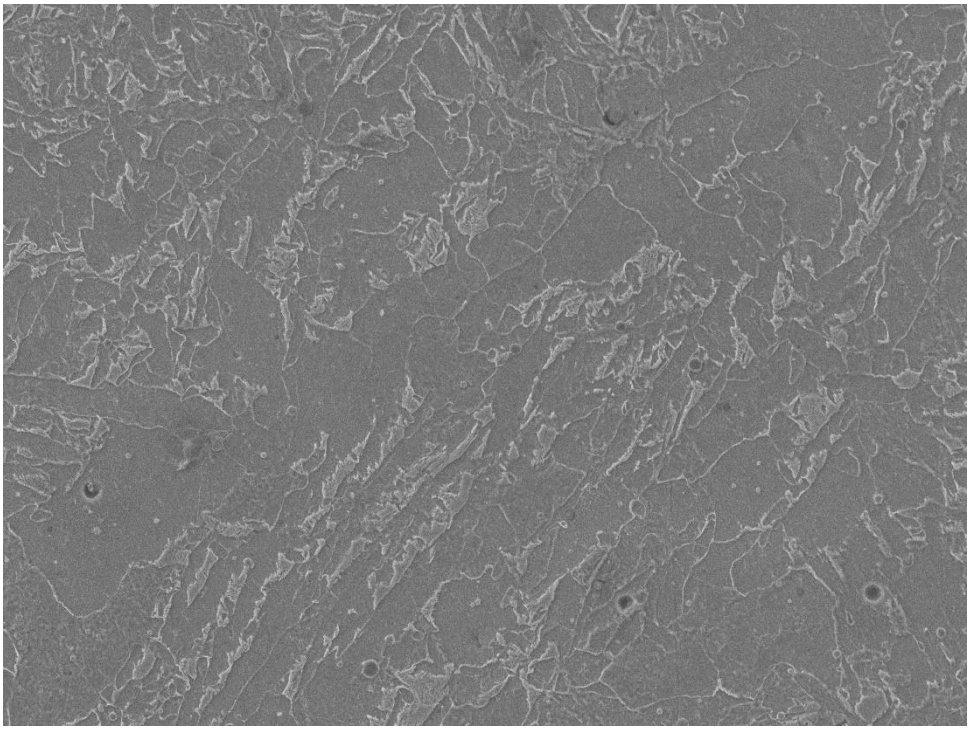

Figure 39. 350A WZ SEM Image at 350x Magnification

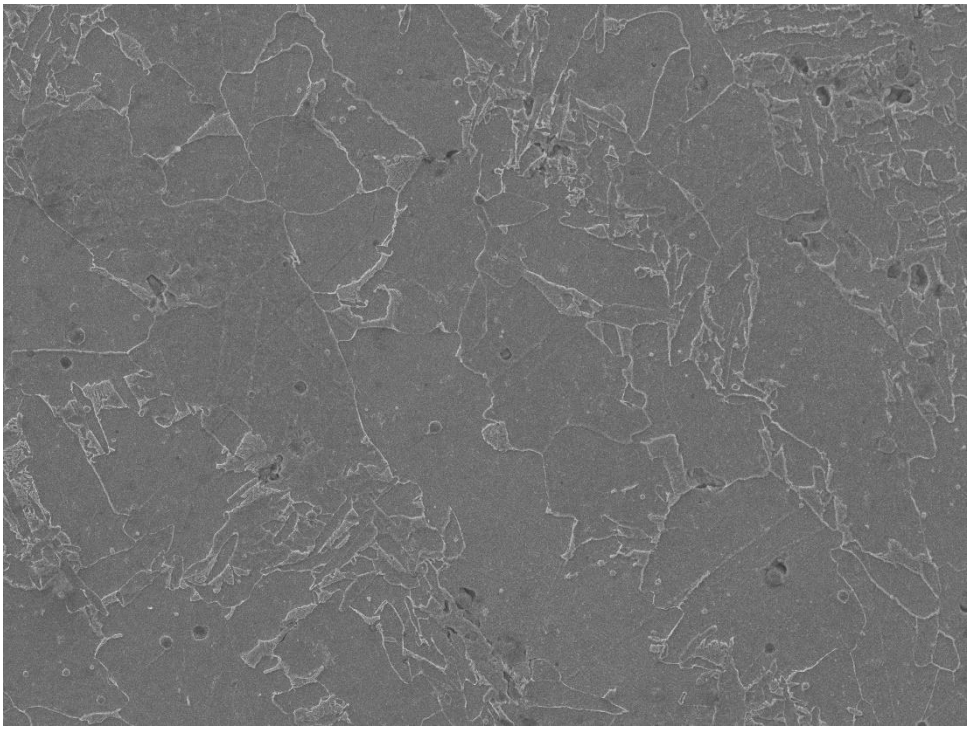

Figure 40. 390A WZ SEM Image at 350x Magnification

As the welding current increases, the proportion of ferrite in the weld zone also increases. At 280A, the SEM analysis reveals a microstructure predominantly composed of acicular ferrite and polygonal ferrite. With the increase in current to 310A, Widmanstätten ferrite appears alongside acicular ferrite, indicating a shift towards a more plate-like structure. At 350A, the microstructure exhibits a mix of acicular ferrite, Widmanstätten ferrite, and grain boundary ferrite, suggesting variations in cooling rates. Finally, at 390A, Widmanstätten ferrite and grain boundary ferrite become more prominent, with coarser grain sizes indicating higher heat input and slower cooling rates. This progression shows that higher welding currents promote the formation of different ferrite morphologies and coarser grains, impacting the weld's toughness, strength, and overall performance. The SEM observations align with optical microscopy findings, underscoring the significant influence of welding current on the weld zone's microstructure.

3.4 EDS analysis:

Energy Dispersive X-ray Spectroscopy (EDS) is a widely used analytical technique for determining the elemental composition of materials. This method leverages the characteristic X-rays emitted from a sample when it is bombarded with an electron beam. By analyzing these X-rays, EDS provides quantitative and qualitative data on the elements present in the sample. Prior to analysis, the samples must be thoroughly cleaned with ethanol to remove any surface contaminants that could affect the accuracy of the results.

The following tables present the results of the EDS analysis for samples welded at different currents:

Table 7 EDS analysis results for 280A weld zone

Element	C	Si	Mn	P	S	Al	Ni	Cu	Mo
Wt.%	0.13	0.27	1.27	0.02	0.005	0.10	0.28	0	0.09

Table 8 EDS analysis results for 310A weld zone

Element	C	Si	Mn	P	S	Al	Ni	Cu	Mo
Wt.%	0.15	0.30	1.28	0	0.005	0.13	0.27	0	0.05

Table 9 EDS analysis results for 350A weld zone

Element	C	Si	Mn	P	S	Al	Ni	Cu	Mo
Wt.%	0.10	0.22	1.18	0	0.005	0.07	0.35	0.01	0

Table 10 EDS analysis results for 390A weld zone

Element	C	Si	Mn	P	S	Al	Ni	Cu	Mo
Wt.%	0.12	0.19	1.23	0.02	0.005	0.05	0.25	0.01	0

The chemical composition obtained from the EDS analysis shows a close resemblance to the base and filler metals used in the welding process. This indicates that the elemental distribution within the weld zones is consistent with the expected composition, confirming the reliability of the welding process. The analysis was conducted on a small area of 2.625 mm^2, providing localized data that is representative of the overall material composition. The slight variations in elemental percentages across different welding currents are within acceptable limits and do not significantly influence the material properties.

3.5 Microhardness test:

The microhardness test measures the hardness of materials on a microscopic scale, providing insight into the material properties at different zones affected by welding. In this study, the Vickers microhardness test was conducted on the weld zone, heat-affected zone (HAZ), and base metal of samples welded at different currents (280A, 310A, 350A, 390A). Measurements were taken to assess the variation in hardness across these zones.

The following graphs show the microhardness distribution across the weld zone, HAZ, and base metal for each welding current. The x-axis represents the distance in millimeters, and the y-axis represents the Vickers hardness (HV).

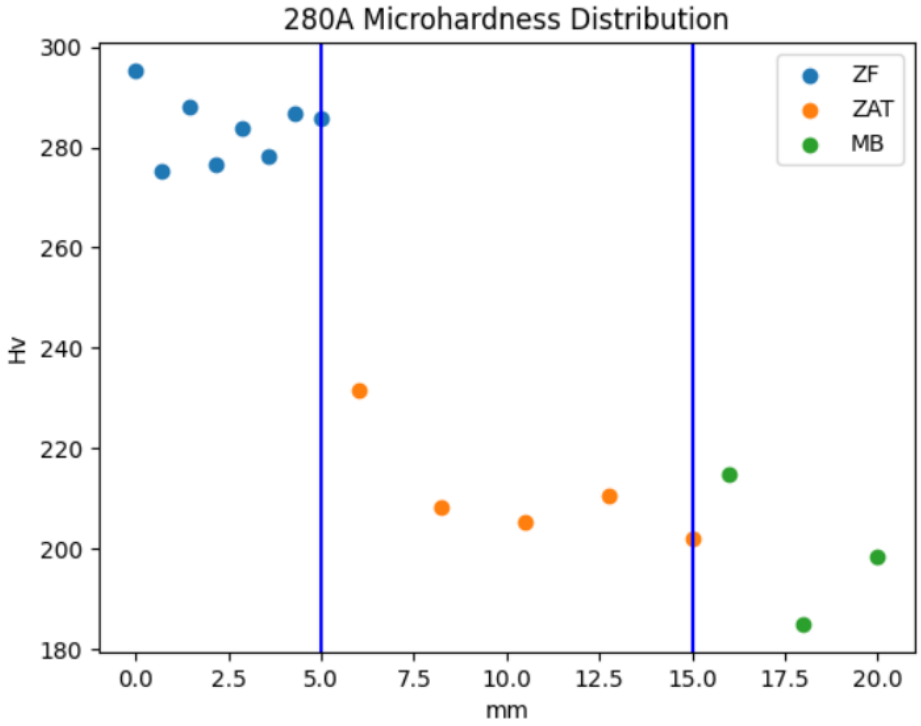

Figure 41. Microhardness Distribution for 280A

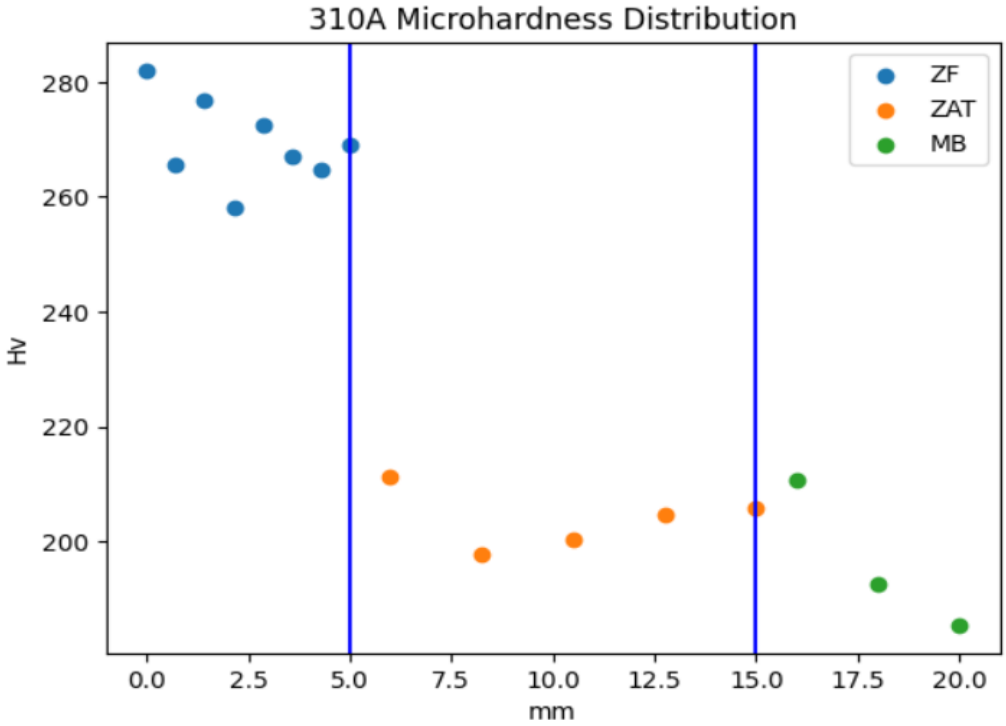

Figure 42. Microhardness Distribution for 310A

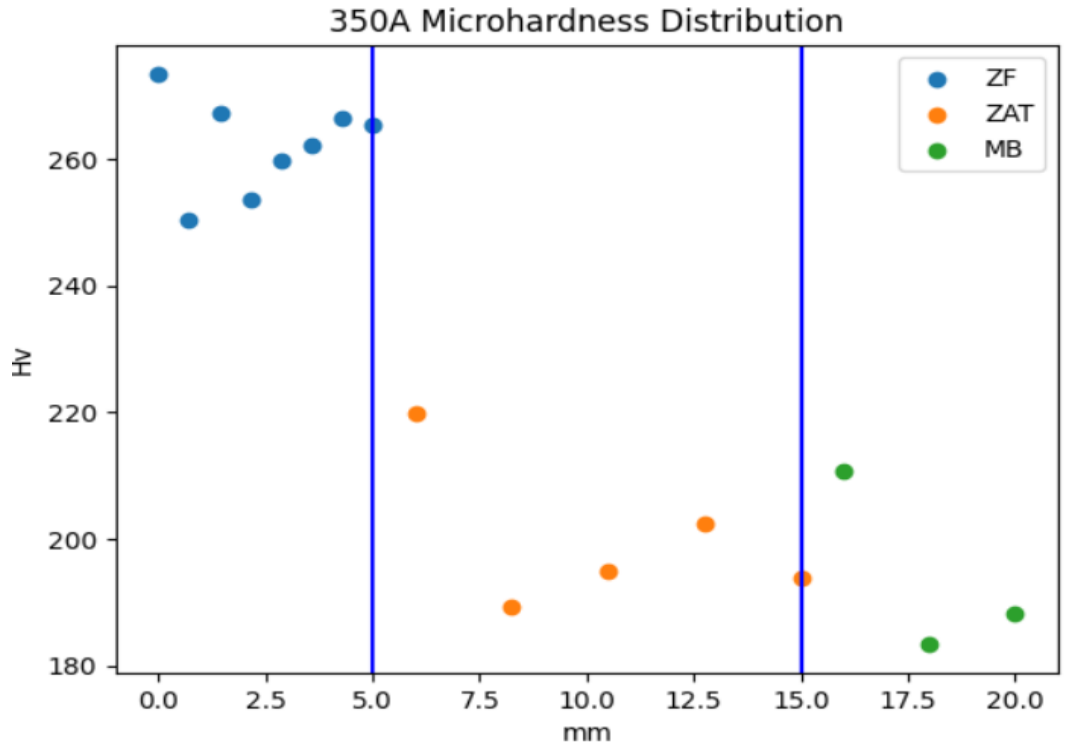

Figure 43. Microhardness Distribution for 350A

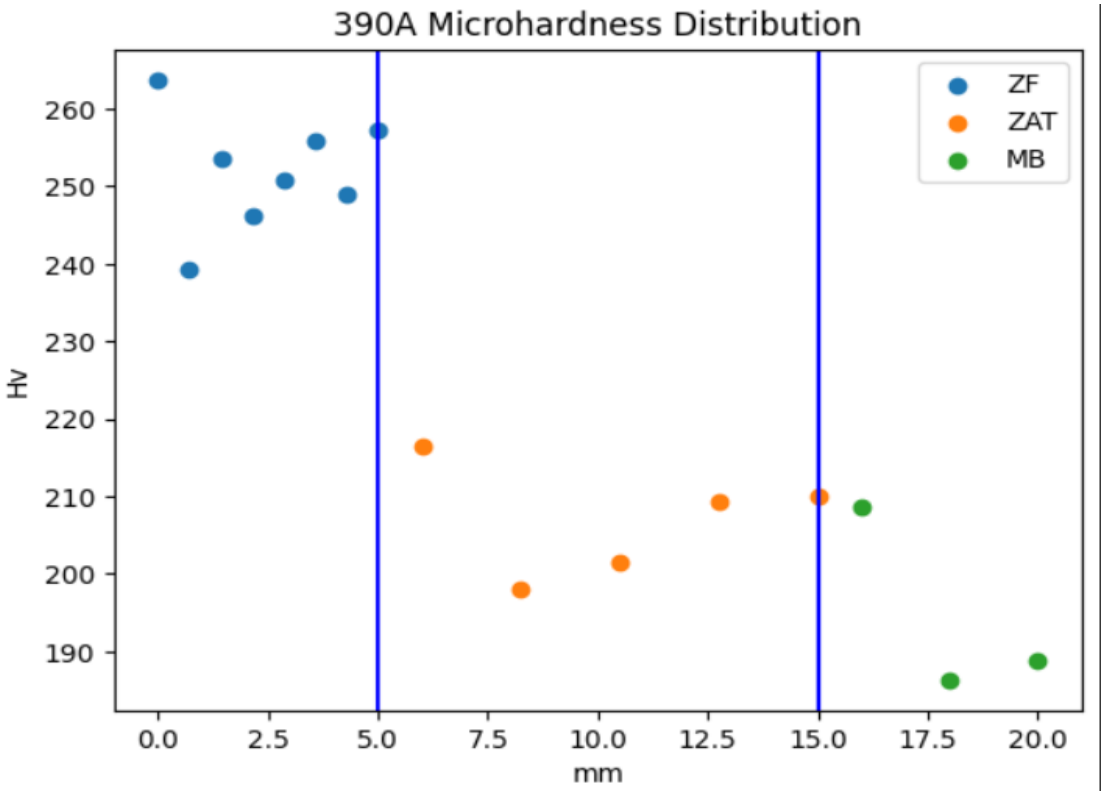

Figure 44. Microhardness Distribution for 390A

The following table presents the average microhardness values for the weld zone, HAZ, and base metal at each welding current.

Table 11 Microhardness Average Values

Amperage	Weld Zone (HV)	HAZ (HV)	Base Metal (HV)
280A	283,15	211,6	199,47
310A	269,64	203,92	196,23
350A	267,05	200,04	194,13
390A	248,94	207,1	194,63

The microhardness test results for the weld zone, heat-affected zone (HAZ), and base metal of samples welded at different currents (280A, 310A, 350A, and 390A) indicate significant variations in hardness across these zones.

Weld Zone: The microhardness in the weld zone decreases as the welding current increases. The highest average microhardness was observed at 280A, with a value of 283.15 HV, while the lowest was at 390A, with a value of 248.94 HV. This reduction in hardness with increasing current suggests that higher currents result in a coarser microstructure with larger grain sizes, leading to lower hardness. This phenomenon is likely due to the increased heat input at higher currents, which promotes grain growth.

Heat-Affected Zone (HAZ): The hardness in the HAZ generally shows a decreasing trend with increasing current, although there are slight fluctuations. At 280A, the HAZ hardness is 211.6 HV, decreasing to 207.1 HV at 390A. The HAZ experiences significant thermal cycles, which affect its microstructure and consequently its hardness. The decrease in hardness indicates that higher currents cause more extensive thermal effects, leading to a softer microstructure in the HAZ.

Base Metal: The base metal hardness values remain relatively stable across different currents, showing less variation compared to the weld zone and HAZ. The hardness values are around 199.47 HV for 280A and slightly lower at 194.63 HV for 390A. This stability suggests that the base metal is not significantly affected by the heat from the welding process, and its microstructure remains unaffected. The heat input during welding primarily influences the weld zone and HAZ, while the base metal retains its original microstructural characteristics.

3.6 Tensile Test:

The tensile test was performed to evaluate the mechanical properties of the welded samples, specifically their tensile strength and elongation. This test helps in understanding the effect of different welding currents on the mechanical performance of the welds. The samples were prepared and tested according to the European standard NF EN 1442, using the Zwick/Roell BT1-EXMACRO.1BL machine. The test results were analyzed using the TestXpert software.

The following graphs illustrate the stress-strain curves for each welding current. The x-axis represents the strain (%), and the y-axis represents the stress (MPa).

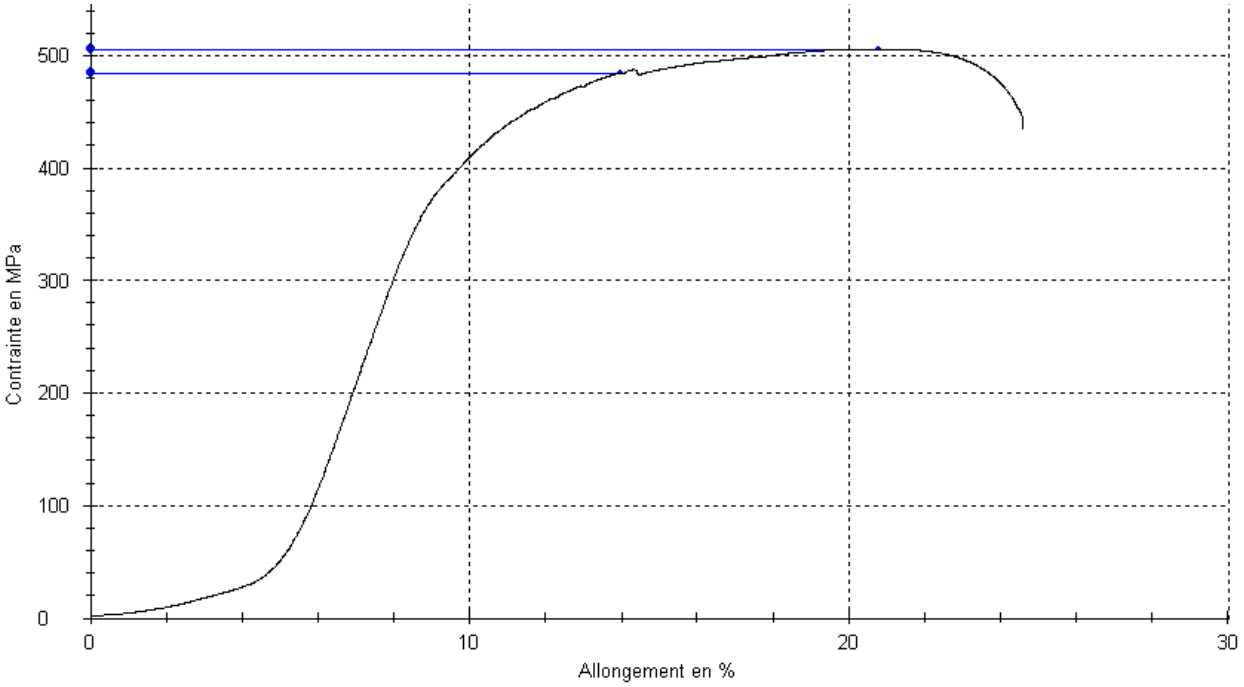

Figure 45. Stress-Strain Curve for 280A

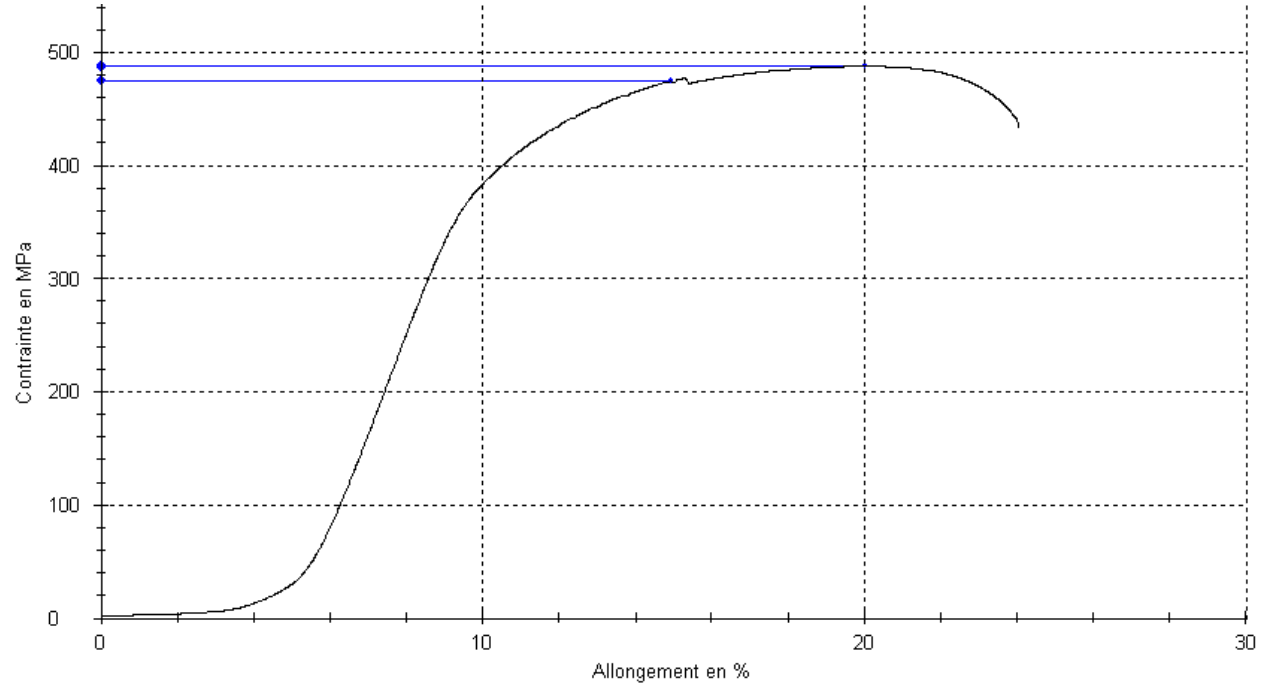

Figure 46. Stress-Strain Curve for 310A

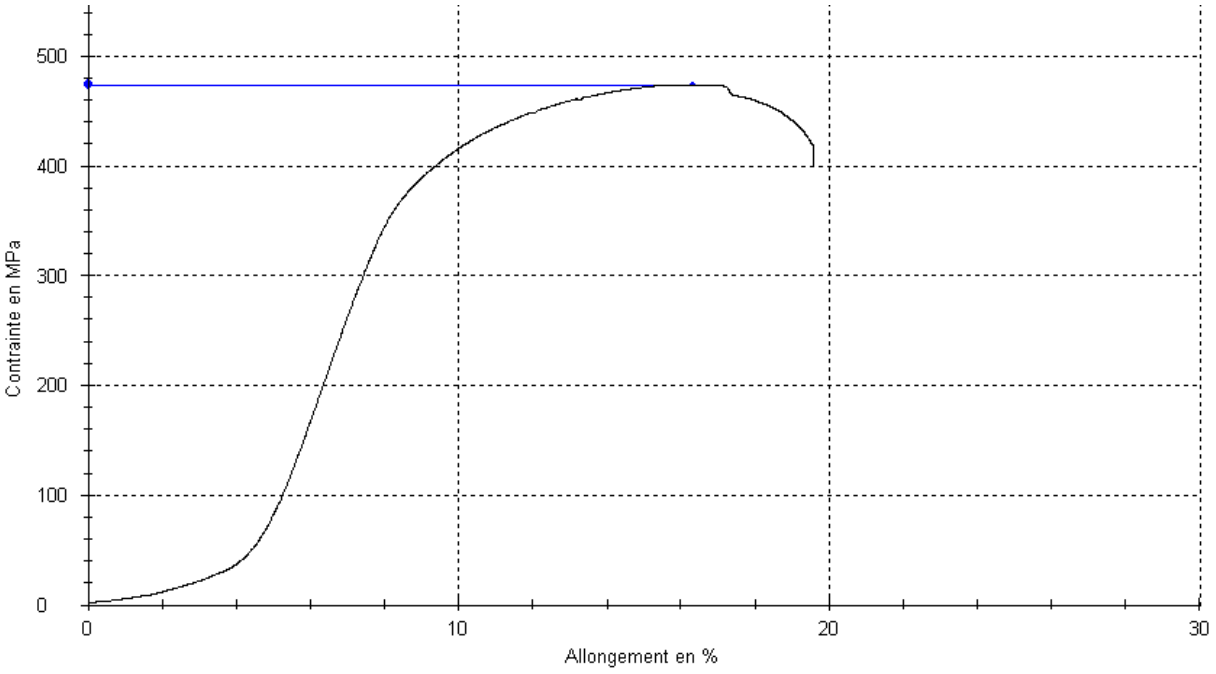

Figure 47. Stress-Strain Curve for 350A

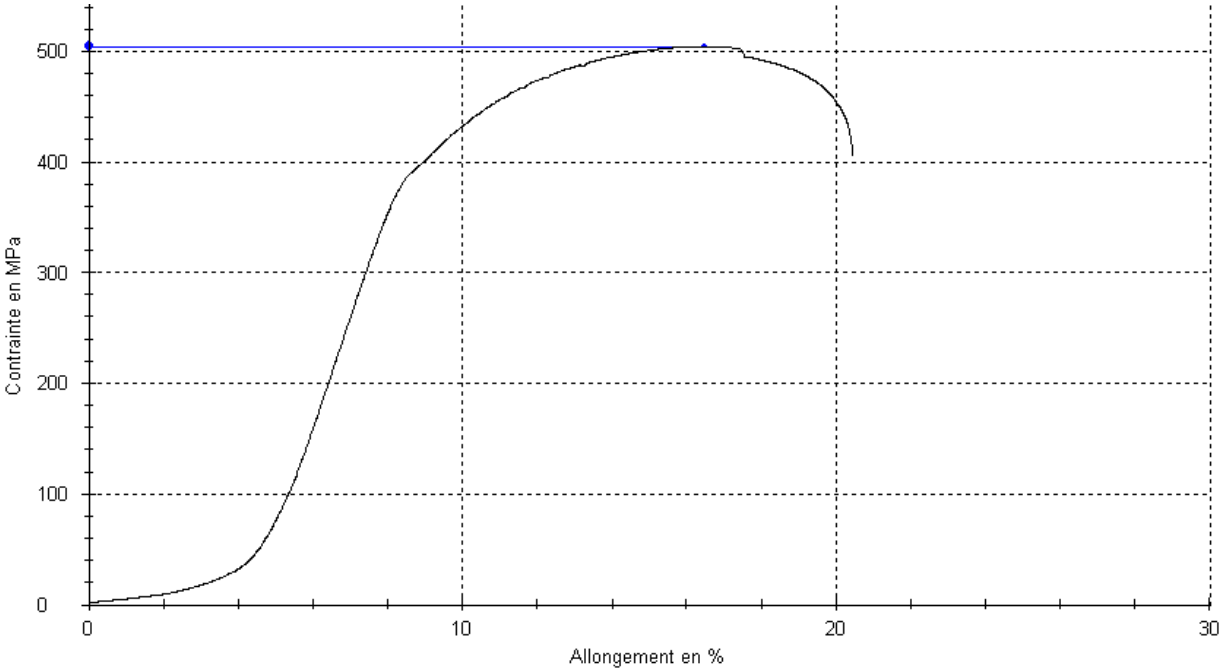

Figure 48. Stress-Strain Curve for 390A

The following table summarizes the average tensile strength and elongation at break for each welding current.

Table 12Tensile Test Results

Amperage	Rm (MPa)	ReH (MPa)	A (%)
280A	506	485	38
310A	488	475	33
350A	474	474	24
390A	504	504	19

It is evident that the yield strength and elongation of the specimens decrease with increasing welding current, indicating a reduction in toughness and ductility of the material after welding. This can be attributed to several factors. The intense heat applied to the weld zone and surrounding areas during welding can cause microstructural changes. In the HAZ, modifications such as recrystallization, the formation of larger grain zones, or phase transformations can occur. These changes can weaken the mechanical properties, including toughness. When larger grains form in the HAZ, they can present a less homogeneous and more

irregular crystalline structure. This altered crystalline structure can reduce the material's ability to absorb plastic deformation energy before fracture, leading to intergranular brittleness and decreased toughness. In other words, larger grains are often less ductile and more brittle.

Regarding tensile strength, it remains almost the same for the different currents, with slight variations that can be attributed to differences in welding process parameters such as welding speed, current intensity, welding wire quality, and operator skill. These factors can all lead to variations in weld properties. Differences in microstructure from one location to another in the same weld, due to material heterogeneity, can also cause variations in tensile strength. Additionally, the way the specimens are prepared for tensile tests can influence the results; misaligned specimens in the testing machine can result in uneven stress and variable outcomes.

It is important to note that the observed fractures occur away from the weld zone, primarily in the base metal, indicating that the weld zone and the HAZ did not act as the weakest points under tensile loading. This suggests a uniform weld quality and a successful welding process. The presence of microporosity or microcracks in the weld zone or HAZ could contribute to this phenomenon. However, in this study, the consistent fracture in the base metal indicates that the welded zones maintained their integrity, highlighting the importance of optimizing welding parameters to achieve the desired mechanical performance.

3.7 XRD test:

In this study, XRD was conducted on the welded samples to analyze the effects of different welding currents (280A, 310A, 350A, 390A) on the microstructure. The samples were prepared and analyzed using a Rigaku MiniFlex600 diffractometer, and the diffraction patterns were recorded.

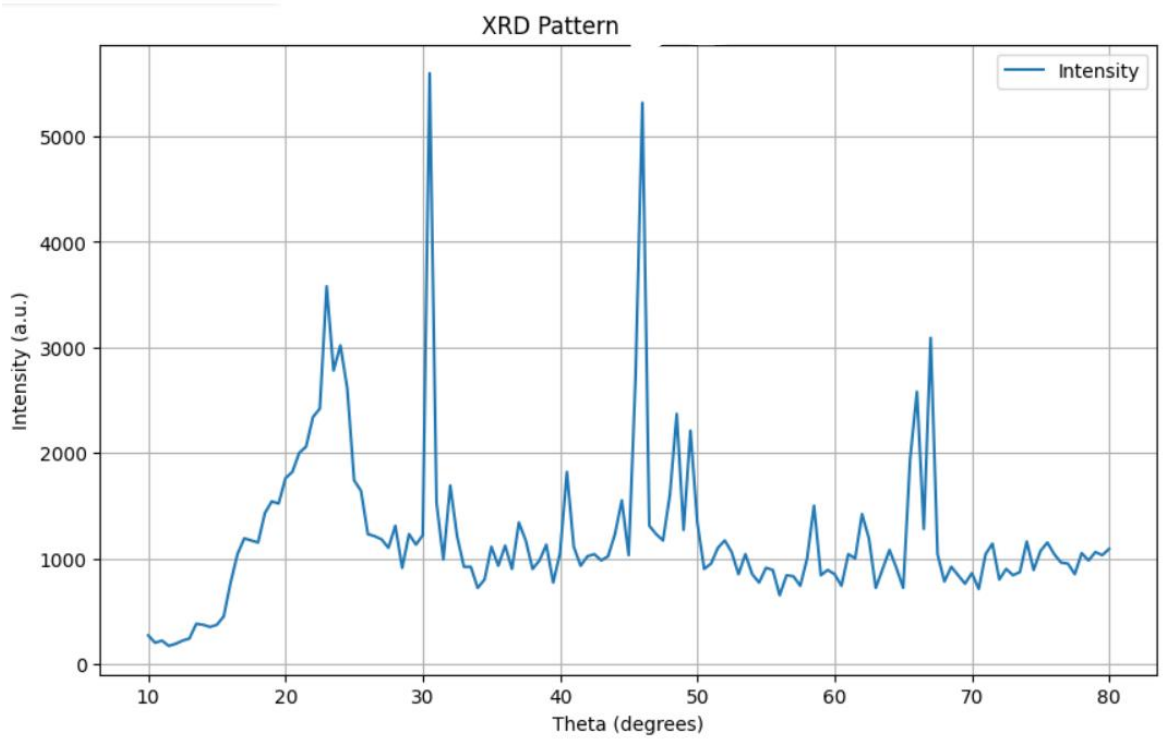

Figure 49. XRD Pattern for 280A Weld Zone

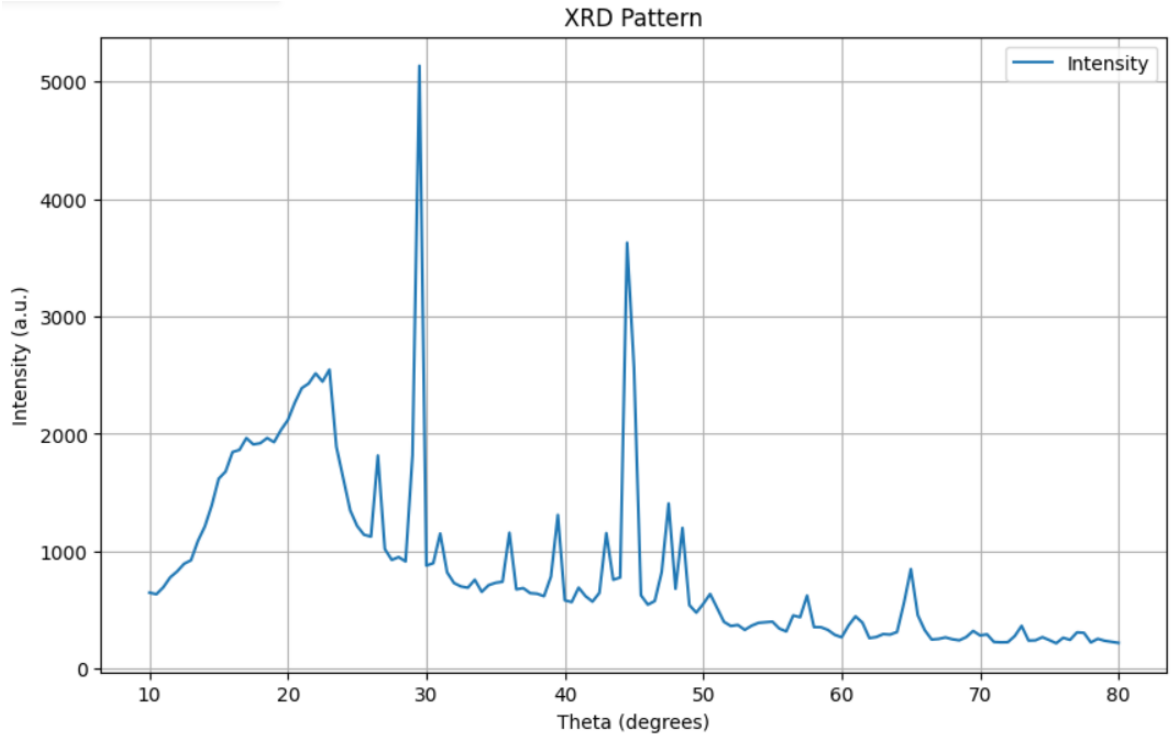

Figure 50. XRD Pattern for 310A Weld Zone

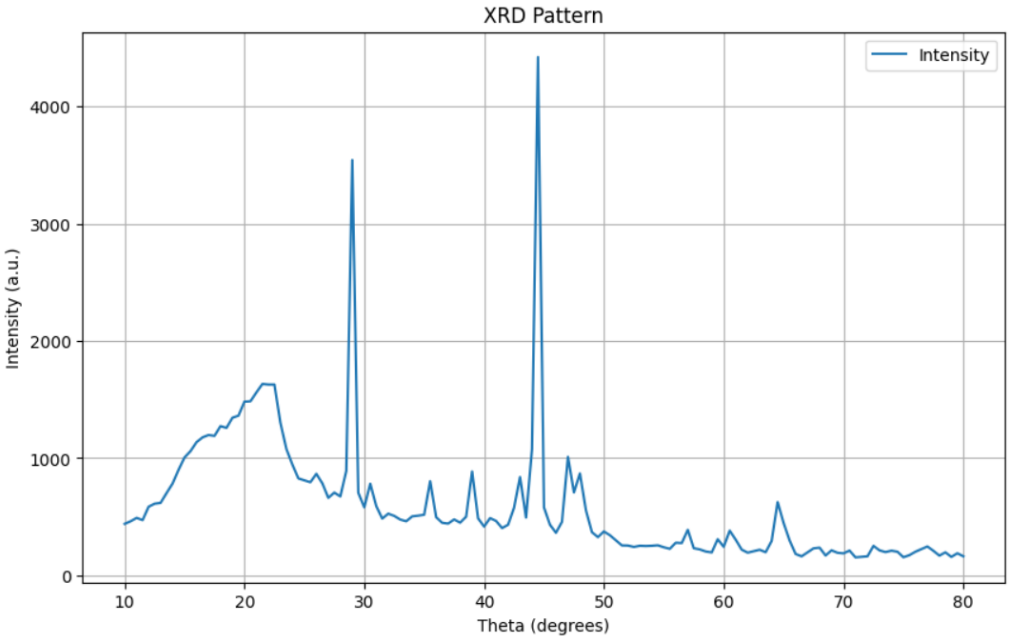

Figure 51. XRD Pattern for 350A Weld Zone

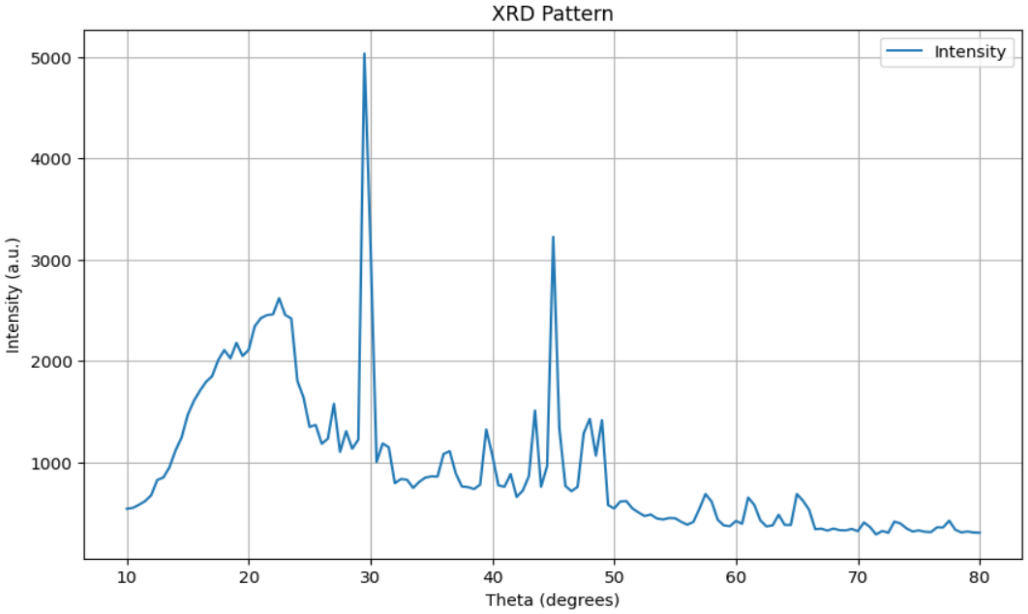

Figure 52. XRD Pattern for 390A Weld Zone

The different peaks in the XRD patterns represent various crystalline phases within the material. The positions of these peaks correspond to specific crystallographic planes, while the intensities provide information about the amount of each phase present. The most prominent peaks in the patterns, which are typically the largest, represent ferrite (α-Fe) crystals. These peaks are indicative of the body-centered cubic (BCC) structure of ferrite, which is the primary phase in steel welds. The smaller peaks in the XRD patterns represent cementite (Fe_3C) phases, which are characteristic of the orthorhombic structure of cementite. The presence of these peaks provides insights into the distribution and proportion of ferrite and cementite in the welded material.

General Conclusion

General Conclusion

In this study, we investigated the influence of varying electrical currents on the microstructure and mechanical properties of steel welds using the Submerged Arc Welding (SAW) method. The research focused on understanding how different welding currents (280A, 310A, 350A, and 390A) affect the weld zone and the heat-affected zone (HAZ) in terms of microstructural transformations and mechanical behavior.

The key findings from the macroscopic examination revealed that increasing welding current leads to wider and deeper weld zones with a more pronounced HAZ. These changes are indicative of the greater heat input associated with higher currents, resulting in more extensive thermal effects on the weld metal and surrounding base metal.

Microscopic examination showed a clear progression in microstructural features with increasing welding current. At lower currents, the weld zone was characterized by a higher proportion of acicular ferrite, contributing to the weld's toughness. As the current increased, the microstructure transitioned to include more Widmanstätten ferrite and grain boundary ferrite, reflecting changes in cooling rates and thermal cycles. This shift towards coarser grains and different ferrite types at higher currents indicates a balance between improved penetration and potential brittleness due to coarser microstructures.

The SEM analysis corroborated these findings, providing detailed images of the microstructures at various currents. The presence of different ferrite morphologies and the coarsening of grains with higher currents were clearly visible, further emphasizing the impact of welding parameters on the microstructure.

The EDS analysis confirmed that the elemental composition of the weld zones remained consistent with the base and filler metals, validating the reliability of the welding process. The slight variations in elemental percentages were within acceptable limits, ensuring that the mechanical properties were not significantly affected by compositional changes.

Mechanical testing through microhardness and tensile tests provided additional insights into the effects of welding currents. The microhardness test revealed a decrease in hardness in the weld zone with increasing current, while the HAZ showed more stable values. The tensile test results indicated a decrease in yield strength and elongation at higher currents, highlighting the trade-off between penetration depth and mechanical performance.

Overall, this study demonstrates that welding current is a critical parameter in SAW that significantly influences the microstructure and mechanical properties of steel welds. By optimizing welding currents, it is possible to achieve a desirable balance between weld penetration, microstructural characteristics, and mechanical performance. The findings of this research contribute valuable knowledge for improving welding practices and enhancing the quality and durability of steel welds in industrial applications.

Bibliography

1. Hosford, W. F. (2012). *Iron and steel*. Cambridge University Press.

2. Cameron, Ian, Chris Davenport, and John Sinclair. *Blast Furnace Ironmaking*. Springer, 2015.

3. Bailey Metal Processing. (2017, September 28). *Chemical composition of steel*. Retrieved from https://www.baileymetalprocessing.com/techmatters/blog-category-1/2017/09/28/chemical-composition-of-steel

4. United States Steel Corporation. (2003). *The Making, Shaping, and Treating of Steel* (11th ed.). AISE Steel Foundation.

5. Liu, Q., Cho, J.-W., & Pereloma, E. (2021). Editorial: Advances in Steel Manufacturing and Processing. *Frontiers in Materials*, 8, Article 708572. https://doi.org/10.3389/fmats.2021.708572

6. Guthrie, R. I. L., & Isac, M. M. (2022). Continuous casting practices for steel: Past, present and future. *Metals, 12*(5), 862. https://doi.org/10.3390/met12050862

7. Dossett, J., & Totten, G. E. (Eds.). (2013). *ASM Handbook, Volume 4A: Steel Heat Treating Fundamentals and Processes*. ASM International.

8. Bertolini, L., Elsener, B., Pedeferri, P., Polder, R. (2004). *Corrosion of Steel in Concrete: Understanding, Investigation and Repair*.

9. Easterling, K. (1992). *Introduction to the Physical Metallurgy of Welding*.

10. Kuziak, R., Cheng, Y. W., Glowacki, M., & Pietrzyk, M. (1997). *Modeling of the microstructure and mechanical properties of steels during thermomechanical processing*. National Institute of Standards and Technology (NIST).

11. Al-Masoudy, M. M. (n.d.). *Engineering Materials* [Class lecture]. Mustaqbal College.

12. Verhoeven, J. D. (2007). *Steel Metallurgy for the Non-Metallurgist*. ASM International.

13. Verhoeven, J. D. (2007). *Steel Metallurgy for the Non-Metallurgist*. ASM International.

14. Bhadeshia, H. K. D. H., & Honeycombe, R. W. K. (2017). *Steels: Microstructure and Properties* (4th ed.). Butterworth-Heinemann.

15. Kou, S. (2003). *Welding Metallurgy* (2nd ed.). Wiley-Interscience.

16. Jeffus, L. (2016). *Welding: Principles and Applications* (8th ed.). Cengage Learning.

17. MSVS-DEI Virtual Labs. (n.d.). *Formation of the Welding Bead*. Retrieved from https://msvs-dei.vlabs.ac.in/mem103/Unit4lesson1.html

18. Ouallam, S. (2009). *Study of TIG and Nd-YAG laser welding of 2024 T3 aluminum alloy* (Master's thesis). National Polytechnic School, Algiers.

19. Houldcroft, P. T. (1989). *Submerged-Arc Welding*. Woodhead Publishing.

20. Lincoln Electric. (n.d.). *Submerged Arc Welding Equipment*.

21. Althouse, A. D., Turnquist, C. H., & Bowditch, W. A. (2013). *Modern Welding* (11th ed.). Goodheart-Willcox.

22. Lee, C. S., Chandel, R. S., & Seow, H. P. (n.d.). Effect of Welding Parameters on the Size of Heat Affected Zone of Submerged Arc Welding.

23. Prasad, K., & Dwivedi, D. K. (2006). Some investigations on microstructure and mechanical properties of submerged arc welded HSLA steel joints. *International Journal of Advanced Manufacturing Technology, 36*(5-6), 475-483. https://doi.org/10.1007/s00170-006-0860-5

24. Kumar, P., Batish, A., Bhattacharya, A., & Duvedi, R. K. (2010). *Effect of process parameters on microhardness and microstructure of heat affected zone in submerged arc welding*. Journal of Engineering Manufacture, DOI: 10.1243/09544054JEM2143

25. Garg, J., Garg, S. B., Jeet, B., & Singh, H. (2022). The effects of flux particle size and column height on the bead geometry in submerged arc welding. *Sadhana*, 47(3), Article 71. https://doi.org/10.1007/s12046-022-01971-7

26. Barot, R. S., & Patel, V. J. (2022). Development and Investigations of IoT Enabled Wire Feed and Weld Speed Measurement for Submerged Arc Welding. *Mapan - Journal of Metrology Society of India, 37*(9). https://doi.org/10.1007/s12647-022-00601-1

27. Thakur, S. (2020). Effect of Welding Parameter of Flux Consumption in Submerged Arc Welding. *SSRN Electronic Journal*. https://doi.org/10.2139/ssrn.3572588

28. Cullity, B. D., & Stock, S. R. (2014). *Elements of X-Ray Diffraction* (3rd ed.). Pearson New International Edition.

29. Suwandi, Y. S. (2024). Effect of Welding Heat Input on the Mechanical Properties of Mild Steel at Coarse Grain Heat Affected Zone (CGHAZ). *Journal of Advanced Research in Applied Mechanics*. https://doi.org/10.37934/aram.116.1.145155

30. Zhou, W., & Wang, Z. L. (2007). *Scanning Microscopy for Nanotechnology: Techniques and Applications*. Springer.

31. Goldstein, J., Newbury, D. E., Michael, J. R., Ritchie, N. W., Scott, J. H., & Joy, D. C. (2017). *Scanning Electron Microscopy and X-Ray Microanalysis* (4th ed.). Springer.

32. Austénite. (n.d.). In Wikipedia. Retrieved June 30, 2024, from https://fr.wikipedia.org/wiki/Aust%C3%A9nite

33. Hamada, S., Sasaki, D., Ueda, M., & Noguchi, H. (2011). Fatigue limit evaluation considering crack initiation for lamellar pearlitic steel. Procedia Engineering, 10, 245-252. https://doi.org/10.1016/j.proeng.2011.04.245

34. Core Materials. (2009, August 25). Martensite microstructure [Photograph]. Flickr. https://www.flickr.com/photos/core-materials/3839976168

35. Viardin, A. (2010). Modélisation par champ de phases de la croissance de la ferrite allotriomorphe dans les aciers Fe-C-Mn (Doctoral thesis). Institut National Polytechnique de

Lorraine, École Doctorale EMMA, Laboratoire de Science et Génie de Matériaux et de Métallurgie.

36. DoITPoMS. (n.d.). Martensite. Retrieved June 30, 2024, from https://www.doitpoms.ac.uk/miclib/micrograph_record.php?id=267

37. DoITPoMS. (n.d.). Austenite. Retrieved June 30, 2024, from https://www.doitpoms.ac.uk/miclib/micrograph.php?id=250

38. DoITPoMS. (n.d.). Lamellar Pearlite. Retrieved June 30, 2024, from https://www.doitpoms.ac.uk/miclib/micrograph.php?id=211